

# *Radiance simulations in support of climate services*

Article

Published Version

Creative Commons: Attribution 4.0 (CC-BY)

Open Access

Poli, P., Roebeling, R., John, V. O., Doutriaux-Boucher, M., Schultz, J., Lattanzio, A., Petraityte, K., Grant, M., Hanschmann, T., Onderwaater, J., Sus, O., Huckle, R., Coppens, D., Theodore, B., August, T., Simmons, A. J., Bell, W., Mittaz, J., Hall, T., Vidot, J., Brunel, P., Johnson, J. E., Zamkoff, E. B., Al-Jazrawi, A. F., Esfandiari, A. E., Gerasimov, I. V. and Kobayashi, S. (2023) Radiance simulations in support of climate services. *Earth and Space Science*, 10 (10). e2023EA002868. ISSN 2333-5084 doi: 10.1029/2023ea002868 Available at <https://centaur.reading.ac.uk/112634/>

It is advisable to refer to the publisher's version if you intend to cite from the work. See [Guidance on citing](#).

To link to this article DOI: <http://dx.doi.org/10.1029/2023ea002868>

Publisher: American Geophysical Union

All outputs in CentAUR are protected by Intellectual Property Rights law, including copyright law. Copyright and IPR is retained by the creators or other copyright holders. Terms and conditions for use of this material are defined in the [End User Agreement](#).

[www.reading.ac.uk/centaur](http://www.reading.ac.uk/centaur)

**CentAUR**

Central Archive at the University of Reading

Reading's research outputs online

# Earth and Space Science



## RESEARCH ARTICLE

10.1029/2023EA002868

<sup>†</sup>Retired

### Key Points:

- Radiance simulations can help characterize two essential inputs of climate services, satellite data records and reanalyses
- Uncertainties in observations collected by the Spektrometer Interferometer-1 flown on a Soviet satellite in 1979 were estimated
- Radiance simulations of satellite instruments can provide information on the quality and realism of climate reanalyses

### Supporting Information:

Supporting Information may be found in the online version of this article.

### Correspondence to:

P. Poli,  
[paul.poli@ecmwf.int](mailto:paul.poli@ecmwf.int)

### Citation:

Poli, P., Roebeling, R., John, V. O., Doutriaux-Boucher, M., Schulz, J., Lattanzio, A., et al. (2023). Radiance simulations in support of climate services. *Earth and Space Science*, 10, e2023EA002868. <https://doi.org/10.1029/2023EA002868>

Received 3 FEB 2023

Accepted 30 JUN 2023

### Author Contributions:

**Conceptualization:** P. Poli, R. Roebeling, V. O. John, J. Schulz, B. Bell

**Data curation:** P. Poli, A. Lattanzio, K. Petraityte, M. Grant, T. Hanschmann, J. Onderwaater, O. Sus, D. Coppens, B. Theodore, T. August, J. Mittaz, J. E. Johnson, E. B. Zamkoff, A. F. Al-Jazrawi, A. E. Esfandiari, I. V. Gerasimov

**Formal analysis:** P. Poli, T. Hanschmann, J. Mittaz, T. Hall

© 2023. The Authors. This article has been contributed to by U.S. Government employees and their work is in the public domain in the USA.

This is an open access article under the terms of the [Creative Commons Attribution License](https://creativecommons.org/licenses/by/4.0/), which permits use, distribution and reproduction in any medium, provided the original work is properly cited.

## Radiance Simulations in Support of Climate Services

P. Poli<sup>1,2</sup> , R. Roebeling<sup>3</sup> , V. O. John<sup>3</sup> , M. Doutriaux-Boucher<sup>3</sup> , J. Schulz<sup>3</sup> , A. Lattanzio<sup>3</sup> , K. Petraityte<sup>3</sup> , M. Grant<sup>3</sup> , T. Hanschmann<sup>3</sup> , J. Onderwaater<sup>3</sup> , O. Sus<sup>3</sup> , R. Huckle<sup>3</sup> , D. Coppens<sup>3</sup> , B. Theodore<sup>3</sup> , T. August<sup>3</sup> , A. J. Simmons<sup>1</sup> , B. Bell<sup>1</sup> , J. Mittaz<sup>4</sup> , T. Hall<sup>5,6</sup> , J. Vidot<sup>7</sup> , P. Brunel<sup>7,†</sup> , J. E. Johnson<sup>8,9</sup> , E. B. Zamkoff<sup>8,10</sup> , A. F. Al-Jazrawi<sup>8,10</sup> , A. E. Esfandiari<sup>8,9</sup> , I. V. Gerasimov<sup>8,9</sup> , and S. Kobayashi<sup>11</sup>

<sup>1</sup>European Centre for Medium-Range Weather Forecasts (ECMWF), Bonn, Germany, <sup>2</sup>Now at European Organisation for the Exploitation of Meteorological Satellites (EUMETSAT), Darmstadt, Germany, <sup>3</sup>European Organisation for the Exploitation of Meteorological Satellites (EUMETSAT), Darmstadt, Germany, <sup>4</sup>University of Reading, Reading, UK, <sup>5</sup>Now at University of Reading, Reading, UK, <sup>6</sup>Space Science & Algorithmics (SPASCIA), Ramonville Saint-Agne, France, <sup>7</sup>CNRM, Université de Toulouse, Météo-France, CNRS, Lannion, France, <sup>8</sup>NASA Goddard Space Flight Center (GSFC), Goddard Earth Sciences Data and Information Services Center (GES DISC), Greenbelt, MD, USA, <sup>9</sup>ADNET Systems, Inc., Bethesda, MD, USA, <sup>10</sup>Telophase Corporation, Greenbelt, MD, USA, <sup>11</sup>Japan Meteorological Agency (JMA), Tokyo, Japan

**Abstract** Climate services are largely supported by climate reanalyses and by satellite Fundamental (Climate) Data Records (F(C)DRs). This paper demonstrates how the development and the uptake of F(C)DR benefit from radiance simulations, using reanalyses and radiative transfer models. We identify three classes of applications, with examples for each application class. The first application is to validate assumptions during F(C)DR development. Hereto we show the value of applying advanced quality controls to geostationary European (Meteosat) images. We also show the value of a cloud mask to study the spatio-temporal coherence of the impact of the Mount Pinatubo volcanic eruption between Advanced Very High Resolution Radiometer (AVHRR) and the High-resolution Infrared Radiation Sounder (HIRS) data. The second application is to assess the coherence between reanalyses and observations. Hereto we show the capability of reanalyses to reconstruct spectra observed by the Spektrometer Interferometer (SI-1) flown on a Soviet satellite in 1979. We also present a first attempt to estimate the random uncertainties from this instrument. Finally, we investigate how advanced bias correction can help to improve the coherence between reanalysis and Nimbus-3 Medium-Resolution Infrared Radiometer (MRIR) in 1969. The third application is to inform F(C)DR users about particular quality aspects. We show how simulations can help to make a better-informed use of the corresponding F(C)DR, taking as examples the Nimbus-7 Scanning Multichannel Microwave Radiometer (SMMR), the Meteosat Second Generation (MSG) imager, and the Defense Meteorological Satellite Program (DMSP) Special Sensor Microwave Water Vapor Profiler (SSM/T-2).

## 1. Introduction

Recognizing increased inter-relations between human activities, impacts, and evolving climate phenomena, the World Climate Conference-3 (WCC-3, 2009a) fostered a substantial expansion and enhancement of climate services worldwide. Although several World Meteorological Organization (WMO) members already operated climate services before 2009, this conference was a milestone in the establishment of the Global Framework for Climate Services (GFCS). In coordination with several other organizations, including the United Nations Educational, Scientific and Cultural Organization (UNESCO), the United Nations Environment Programme, the Food and Agriculture Organization of the United Nations (FAO), and the International Council for Science (ICSU), the GFCS was established to complement and support the work of the Intergovernmental Panel on Climate Change (IPCC) and the United Nations Framework Convention on Climate Change (UNFCCC) (WCC-3, 2009b).

More than 10 years later, climate services have evolved beyond the scope of classical climatology. Moving on from the form of climate means, compiled and served to the public by national weather agencies, climate activities today embrace a bundle of relationships and exchanges between the climate data and actors and societal applications (e.g., Bresseur & Gallardo, 2016). Furthermore, environmental observations are no longer the exclusive remit of selected public agencies: observations are now collected, assembled, curated, and served by a variety of actors including, for example, space agencies, universities, research programs and organizations involved in environmental monitoring, but also associative or private initiatives, and structural elements such as cloud-computing

**Funding acquisition:** V. O. John, J. Schulz, B. Bell  
**Investigation:** P. Poli, V. O. John, M. Doutriaux-Boucher, T. Hanschmann, J. Mittaz, T. Hall, S. Kobayashi  
**Methodology:** P. Poli, R. Roebeling, V. O. John, M. Doutriaux-Boucher, J. Schulz, T. Hanschmann, B. Bell, J. Mittaz, J. Vidot, P. Brunel  
**Project Administration:** J. Schulz, M. Grant, B. Bell  
**Resources:** A. Lattanzio, K. Petraityte, M. Grant, T. Hanschmann, J. Onderwaater, O. Sus, R. Huckle, D. Coppens, B. Theodore, T. August, J. Vidot, P. Brunel  
**Software:** P. Poli, V. O. John, T. Hanschmann, J. Onderwaater, J. Mittaz, J. Vidot, P. Brunel  
**Supervision:** J. Schulz  
**Validation:** P. Poli, T. Hanschmann, J. Mittaz, S. Kobayashi  
**Visualization:** P. Poli, V. O. John, J. Mittaz  
**Writing – original draft:** P. Poli, A. J. Simmons, J. Mittaz  
**Writing – review & editing:** P. Poli, R. Roebeling, V. O. John, M. Doutriaux-Boucher, M. Grant, R. Huckle, T. August, A. J. Simmons, B. Bell, J. Vidot, P. Brunel, S. Kobayashi

platforms (e.g., Thorpe & Rogers, 2018). These actors operate alongside traditional national weather agencies that remain, in most cases, ultimately responsible for key properties of Climate Data Record (CDR) monitoring (Mahon et al., 2019).

Climate monitoring is only one component of climate services (World Meteorological Organization (WMO), 2018). Other components, of which some of them are related to monitoring, include climate reanalyses, climate indicators and indices, longer-term forecast elements that include predictions and projections, and attribution of climate phenomena. This last component is crucial to understand the causes of, and later better project or predict, selected climate phenomena and their impacts, and develop relevant mitigation or adaptation measures. Enabled by methods such as developed by Hasselmann (1997), attribution is a preliminary step before further climate adaptation or mitigation measures may be taken. Attribution is also called to play a role in the UNFCCC Warsaw International Mechanism to deal with loss and damage due to climate change (Parker et al., 2015). Beyond this, without an underlying understanding of the causes of important climate phenomena (such as “extremes”) and their inter-relations with human activities, the risks run high of counter-productive societal measures that can worsen the issues at stake (e.g., Schipper, 2020).

Even if climate services are not limited to climate monitoring and the corresponding preparation and provision of observation-based CDRs, these data records remain the necessary physical basis for all other components of the climate services (World Meteorological Organization (WMO) & European Commission, 2015). As such, observation-based products underpin the outcomes of IPCC's First Working Group that examines the physical science of climate change (Masson-Delmotte et al., 2021). Similarly, observations are often depicted at the onset of the weather and climate value chain (e.g., Ruti et al., 2020).

The present paper focuses on a method to accelerate the development and uptake of satellite-based CDRs. These are optimally based on satellite sensor data in the form of Fundamental Climate Data Records (FCDRs), or else on Fundamental Data Records, also referred to as Sensor Data Records (Privette et al., 2023). Hereafter we evaluate the quality of F(C)DRs by comparing them with simulated observations. While the use of simulations to survey the quality of satellite-based observations and products over the long-term is not a novelty (e.g., Gibson et al., 1997; Jackson & Soden, 2007; Newman et al., 2020), their use to support the CDR development is rather recent.

The outline of this paper is as follows. Section 2 presents the data and methodology. Sections 3–5 showcase three different classes of applications, namely, Class-I: validating assumptions (Section 3), Class-II: assessing coherence between observations and reanalyses (Section 4), and Class-III: informing users (Section 5). Section 6 discusses the results. Finally, Section 7 presents conclusions and prospects for future work.

## 2. Data and Methodology

Satellite observations considered in this paper come from several instruments. The radiative transfer simulations use reanalysis fields as input, and provide in return brightness temperatures (or reflectances), for microwave channels and visible, near-infrared, shortwave infrared, and thermal infrared channels. The differences between the observations and simulations are hereafter called departures. The methods and data used in the paper are presented below.

### 2.1. Radiative Transfer Simulations

Since the early days of satellite meteorology, the accurate and faithful numerical simulation of satellite measurements has been a topic of research and active development (e.g., Gordon, 1962). From early on, the simulation methods for radiative transfer have involved a mix of exact solutions and numerical methods (e.g., Hunt & Grant, 1969; Rodgers & Walshaw, 1963). A representation of the so-called direct (or forward) model is an essential tool to exploit the measurements and map the signals into useful information (e.g., Rodgers, 1990). Also, by allowing physical quantities to be estimated from the measurements, such as inversion or retrieval process (e.g., Stephens, 1994), any improvement to the forward models further helps to enhance the understanding of the observed natural phenomena (e.g., Houborg & McCabe, 2016).

Simulations of satellite observations have proven to bring about additional benefits, in line with the continuous development in Earth sciences. This is an iterative process where the lessons learned from the confrontation of simulation results with actual observations enhance our understanding of important effects affecting the quality

the observations, thereby allowing to repeat the data processing or simulations with improved algorithms, or to improve future instrument design. This was shown, in particular, for the physical interactions between the observed phenomena and the measurement process (e.g., W. Bell et al., 2010; John & Buehler, 2004; Joiner & Poli, 2005). These iterative improvements enable researchers to continue extracting ever-increasing value from these observations for societal applications, such as Numerical Weather Prediction (e.g., Shahabadi et al., 2018). Furthermore, such enhanced understanding also helps to refine the design of new-generation instruments or data records. This allows, for example, better understanding instrument aging processes (e.g., Munro et al., 2016; Quast et al., 2019), detecting the impact of imperfections that were previously thought negligible (e.g., Lu & Bell, 2014), or releasing new versions of the data records that correct for observation sampling effects (e.g., Mears & Wentz, 2017). Another benefit is to enhance our understanding of discrepancies between models and observations, especially for data assimilation, whose remit is to exploit these differences to extract information, even when a bias correction procedure is necessary (e.g., Joiner & Rokke, 2000), for applications such as Numerical Weather Prediction (NWP). On longer timescales, quantifying discrepancies between models and observations can also help pinpoint effects that are important to consider in models, such as anthropogenic effects (e.g., De Vrese & Hagemann, 2018).

Alongside all these applications sits also research toward using novel technology instruments (e.g., Doutriaux-Boucher et al., 1998) or to revisit early satellite data records (e.g., Poli et al., 2017). However, climate research presents several distinct challenges when it comes to observation data simulators. First, the time-series covered by climate model and by related satellite-based CDR products are necessarily long. This makes running a full data assimilation system (with underpinning Earth-system models and covering many observation types) an overly computationally-expensive and inadequate venture. This is also partly unnecessary in the face of the efforts already deployed by large modeling centers to create model-gridded global decadal data sets, such as reanalyses, which gradually widen their remit to exploit (and hence simulate) an increasing diversity of satellite-based data records. Second, the variety of observation data that are available exceeds the variety of data encountered in a single data assimilation window that covers a few hours of a given date. Furthermore, a thorough and relevant assessment of reprocessed satellite data mandates to use state-of-the-art simulators that can be applied to the latest versions of the data records quickly. This timing is not compatible with the planning of reanalyses productions, which take years to prepare and execute. Finally, such assessments require efficient and traceable simulation tools, while maintaining a strong link to community-driven efforts that continually improve such simulation tools, based on the latest science (e.g., Swales et al., 2018).

Owing to these specificities, data simulators can be beneficial in at least three different points of the climate value chain. The first possibility is to use them during the F(C)DR development phase, to validate the assumptions made. A second possibility is to use them after the production of a F(C)DR, but before data release, to assess the realism and coherence between a new F(C)DR and state-of-the-art Earth system reanalyses. A third possibility is post-production, even possibly after a F(C)DR release, to inform the data users about likely sources of variability present in the data (e.g., natural variability vs. instrumental or sampling artifacts). These represent many feed-back opportunities. Note this paper does not discuss the issue of using simulators as integral part of the F(C)DR production chain.

All these potential benefits have contributed to the development of a standalone RADiance SIMulator (RADSIM) (Hocking, 2022), able to simulate all the satellite sensors supported by the Radiative Transfer for Television Infra-red Orbiting Satellite (TIROS) Operational Vertical Sounder (TOVS) (RTTOV, Saunders et al., 2018). It must be recalled that both elements, RADSIM and RTTOV, benefit from a long-term support of the EUMETSAT climate services and development plan, with activities distributed between the EUMETSAT central facility and its Satellite Applications Facility (SAF) network, including the NWP-SAF, for these simulators. The results shown in this manuscript build on an implementation of RADSIM and RTTOV in the EUMETSAT infrastructure, with massively parallel computations carried out on a multi-node cluster computing system.

In the present study, we use RADSIM interfaced with RTTOV version 13.0, except for simulating data from the Medium-Resolution Infrared Radiometer (MRIR) where we used RTTOV version 12.2. Additional details about the radiance simulation configuration are given in Text S1 in Supporting Information S1.

## 2.2. Reanalysis Data

Reanalyses are used for their ability to provide temporally and spatially complete fields of key atmospheric properties. Several global comprehensive reanalyses of the atmosphere have been produced in the recent past. The following are considered in the present work, cited in the order they were released: ERA-Interim (Dee et al., 2011;

ECMWF, 2009), JRA-55 (Japan Meteorological Agency, 2013; Kobayashi et al., 2015), ERA-20C (ECMWF, 2014; Poli et al., 2016), ERA5 (Copernicus Climate Change Service, 2018; Hersbach et al., 2020), and JRA-3Q (Japan Meteorological Agency, 2022; S. Kobayashi et al., 2021). Among these, only ERA5 provides hourly analyses. For all others, the radiative transfer simulator uses 6-hourly analyses. The reanalyses are used at  $0.5^\circ \times 0.5^\circ$  (latitude, longitude) horizontal resolution, except for MRIR simulations that used ERA5 data at  $1^\circ \times 1^\circ$  resolution. The geophysical parameters include temperature, humidity, and ozone (for all available model levels), as well as near-surface wind speed, temperature, and humidity, and surface air pressure, surface geopotential, skin temperature, land-sea mask, and sea-ice cover. The reanalysis cloud and precipitation information is not used in the simulations.

### 2.3. Satellite Data

This work uses data records from eight different satellite instruments:

- Meteosat Visible Infra-Red Imager (MVIRI), flown on Meteosat First Generation (MFG) satellites, Meteosat-2 to -7 (EUMETSAT, 2020),
- Spinning Enhanced Visible and InfraRed Imager (SEVIRI), flown on Meteosat Second Generation (MSG) satellites, Meteosat-8 to -11 (EUMETSAT, 2015)
- MRIR, flown on several TIROS and Nimbus satellites, noting that this study only uses data collected by Nimbus-3 (McCulloch, 2014),
- Spektrometer Interferometer (SI-1), flown on Soviet weather satellites Meteor-28 and -29, noting that this study only uses data collected by Meteor-29 (Poli et al., 2023),
- High-resolution Infrared Radiation Sounder (HIRS), flown on NOAA Polar Operational Environmental Satellites TIROS/N, NOAA-6 to -19 and EUMETSAT polar-orbiting satellites, Metop-A and -B (EUMETSAT, 2022),
- Advanced Very High Resolution Radiometer (AVHRR) flown on the same satellites as HIRS as well as Metop-C (EUMETSAT, 2023),
- Scanning Multichannel Microwave Radiometer (SMMR), flown on satellites Seasat and Nimbus-7, noting that this study only uses data collected by Nimbus-7 (Fennig et al., 2017),
- Special Sensor Microwave Water Vapor Profiler (SSM/T-2), flown on U.S. Defense Meteorological Satellite Program (DMSP satellites F-11, -12, -14, and -15 (EUMETSAT, 2021).

The first two instruments are visible and infrared imagers on geostationary satellites, the next four are visible and/or infrared imagers or infrared sounders on polar-orbiting satellites, and the last two are microwave radiometers on polar-orbiting satellites. Several instruments are historical sensors, given their early data record.

While it would take too long to expand all details of these instruments, as well as their detailed configurations, Table 1 provides a summary of some of their key characteristics. Other references, such as the WMO Observing Systems Capability Analysis and Review tool (OSCAR) Space database (<https://space.oscar.wmo.int>), provide further information for these instruments. Additional instrument information is given later, as relevant, when presenting the simulation applications.

Table 1 indicates if the data records have been used in one way or another in global reanalysis, indicating here the situation only for the data sources assimilated in ERA5 (Hersbach et al., 2020), because it is the only reanalysis used for all comparisons. There are several cases of indirect data use in ERA5, as indicated in Table 1. There are only three cases of direct assimilation of the radiance data considered in the present study into ERA5 (Hersbach et al., 2020): (a) MVIRI after 2001, (b) SEVIRI, and (c) HIRS.

Taking note of this inter-relation between reanalysis and the radiance data records, the following remediation steps are taken. (a) For MVIRI we only show results before the date when MVIRI radiances started being assimilated in ERA5. (b) For SEVIRI we do not simply consider departures (differences between observed radiances and simulations), but consider how they vary by changing the simulation setup. (c) For HIRS we do not consider the departures alone but along with AVHRR, and we also exploit the departures at a time-scale for which we believe there is independence between the satellite data record and the reanalysis.

### 2.4. Quality Controls

#### 2.4.1. Observations

Observations with missing geolocation, brightness temperatures, or reflectances (in the case of AVHRR visible and near-infrared channels) are excluded from further analysis. In addition, specific quality controls are applied

**Table 1**  
Overview of Selected Characteristics for Instruments Considered in the Present Study

Sensor	Years of operation	IFOV size <sup>a</sup> (km)	Scanning pattern	Nb. of channels (wavelengths or frequencies)	DOI <sup>b</sup>
MVIRI <sup>c,d,f</sup>	1977–2017	4.5	Earth disc, every 30 min	2 (6.4, 11.5 $\mu\text{m}$ ) <sup>e</sup>	<a href="https://doi.org/10.15770/EUM_SEC_CLM_0009">https://doi.org/10.15770/EUM_SEC_CLM_0009</a>
SEVIRI <sup>c,d,f</sup>	2002–2023	3	Earth disc, every 15 min	8 (3.9–13.4 $\mu\text{m}$ ) <sup>e</sup>	<a href="https://doi.org/10.15770/EUM_SEC_CLM_0008">https://doi.org/10.15770/EUM_SEC_CLM_0008</a>
MRIR <sup>c,g</sup>	1969–1970	55	85 pixels along 3,000 km swath	4 (6.5–23 $\mu\text{m}$ ) <sup>e</sup>	<a href="https://doi.org/10.5067/XTJ53AK84QRL">https://doi.org/10.5067/XTJ53AK84QRL</a>
SI-1 <sup>c</sup>	1977, 1979	25	Nadir only, every 100 km along-track	579 (6–25 $\mu\text{m}$ )	<a href="https://doi.org/10.15770/EUM_SEC_CLM_0086">https://doi.org/10.15770/EUM_SEC_CLM_0086</a> <sup>h</sup>
HIRS <sup>c,f</sup>	1978–2023	20 <sup>i</sup>	56 pixels along 2,200 km swath	19 (3.7–15 $\mu\text{m}$ ) <sup>e</sup>	<a href="https://doi.org/10.15770/EUM_SEC_CLM_0026">https://doi.org/10.15770/EUM_SEC_CLM_0026</a>
AVHRR <sup>c,d</sup>	1978–2023	1.1 <sup>j</sup>	2,048 pixels <sup>j</sup> along 2,900 km swath	AVHRR/1:4 (0.6–11 $\mu\text{m}$ ), AVHRR/2:5 (0.6–12 $\mu\text{m}$ ), AVHRR/3:6 (idem)	<a href="https://doi.org/10.15770/EUM_SEC_CLM_0060">https://doi.org/10.15770/EUM_SEC_CLM_0060</a>
SMMR <sup>c,d</sup>	1978–1987	20–120	94 pixels along 780 km swath	10 (6.6–37 GHz)	<a href="https://doi.org/10.5676/EUM_SAF_CM/FCDR_MWI/V003">https://doi.org/10.5676/EUM_SAF_CM/FCDR_MWI/V003</a>
SSM/T-2 <sup>c</sup>	1994–2005	48	28 pixels along 1,500 km swath	5 (91–183 GHz)	<a href="https://doi.org/10.15770/EUM_SEC_CLM_0050">https://doi.org/10.15770/EUM_SEC_CLM_0050</a>

Note. Several instruments still operate at the time of writing.

<sup>a</sup>Instantaneous Field-Of-View (IFOV), at the sub-satellite point. <sup>b</sup>Digital Object Identifier (DOI) for the data used in the present work, accessible at <https://doi.org/<DOI>>. <sup>c</sup>More information about this instrument is accessible from WMO OSCAR at <https://space.oscar.wmo.int>. <sup>d</sup>Radiance data from this instrument were indirectly used in ERA5, as follows, via assimilation of atmospheric motion vector (MVIRI, SEVIRI, AVHRR), or as input to the sea-surface temperature forcing (AVHRR) or the sea-ice forcing (SMMR). <sup>e</sup>Visible channels from this instrument are not simulated in the present work. <sup>f</sup>Radiance data from this instrument were assimilated in ERA5. <sup>g</sup>The information given here pertains only to Nimbus-3. <sup>h</sup>This is the DOI reserved for future publication of the entire data record, noting that the subset of data used in the present work are available from <https://doi.org/10.5281/zenodo.7912742>. <sup>i</sup>Except for HIRS/4 (10 km), noting also HIRS on Nimbus-6 is not covered here. <sup>j</sup>Note that AVHRR Global Area Coverage data used in the present work present a lower resolution.

to the data records of each instrument, using the information available. For completeness, the details are reported in Text S1 in Supporting Information S1.

#### 2.4.2. Simulations

The performance of radiative transfer simulations can be degraded in several situations. These are indicated in this sub-section, along with measures to mitigate these degradations.

Performance degradation of the simulations may occur in situations of Non-Local Thermal Equilibrium if this effect is not specifically accounted for. Such degradations, which arise during daytime in modeling short-wave infrared channels, are excluded from the analysis; for the corresponding HIRS, AVHRR, and SEVIRI channels (with wavelengths in the region 3–4  $\mu\text{m}$ ), we follow a conservative approach, retaining only cases when the sun is below the horizon by at least 10°. Similarly, the performance of RTTOV may be degraded for situations of specular reflections. Consequently, in the AVHRR visible and near-infrared channels simulations, cases in which the sun is low on the horizon are discarded from the analysis (we retain only cases when the sun is above the horizon by more than 10°).

The performance of radiative transfer simulations is also degraded when the presence of clouds (infrared and visible) or precipitating clouds (microwave) is not accounted for. As all simulations are carried out assuming clear sky conditions, we need to apply a filtering to exclude cloudy situations (infrared and visible) or precipitating

clouds (microwave). For simplicity, we use the generic term “cloud mask” in all cases, even if there are distinct differences in the implementations. These implementations are described now.

In the absence of a single cloud mask for all instruments at all dates and times, the cloud filtering approach depends on the instrument. The presence of clouds and/or precipitation is filtered in three cases in this study.

In the first case, a cloud mask is available for the instrument's data record. This applies to AVHRR (Karlsson et al., 2023), MVIRI (Stöckli et al., 2019), SEVIRI (EUMETSAT, 2015), and SSM/T-2 (EUMETSAT, 2021). In the case of SSM/T-2, the cloud mask uses information retrieved from Special Sensor Microwave Imager (SSM/I) observations by the EUMETSAT Climate Monitoring SAF (CM-SAF) (Andersson et al., 2017), albeit only available over oceans.

In the second case, the availability of a window channel (i.e., a channel affected only weakly by atmospheric absorption) enables use of the departure window method check, similar to the approach typically employed by data assimilation (e.g., Krzeminski et al., 2009). In this method, a departure outside a predefined range is indicative of the presence of cloud. This method works better over ocean than over land, affected by greater uncertainties in sea-surface temperature and emissivity, and is applied over ocean region for filtering out clouds from SI-1 observations. The range of allowed window channel departures is set to  $(-2\text{ K}, 3\text{ K})$ , as the SI-1 instrument operated before the well-observed satellite era, and when the quality of reanalyses is known to be poorer (e.g., B. Bell et al., 2021). The SI-1 channels considered for this check are between  $882$  and  $916\text{ cm}^{-1}$ .

In the third case, when neither of the two approaches above is applicable, but the effects of clouds or rain need to be filtered out, we devise proxy criteria to identify pixels affected by these situations. These criteria are presented afterward, for MRIR and SMMR.

Additional details on the application of the cloud masks are presented in the relevant sections hereafter as relevant.

## 2.5. Departure Analysis

The general philosophy for analyzing the results is to follow the split-apply-combine method (Wickham, 2011), preceded by the quality control steps mentioned previously. Hereafter, we consider two statistics of the departures (observations minus simulations): the mean (noted  $\mu$ ) and the standard deviation (noted  $\sigma$ ). Both quantities are in K for brightness temperatures, or in % for reflectances (for visible or near-infrared channels).

## 3. Class-I Applications: Validating an Assumption

When developing a data set or an application, it is common to be faced with the issue of validating an assumption used in the methodology. The assumption could, for example, relate to the data themselves, or how to use them. However, a common difficulty is the impracticality of proving the assumption. One can then revert to demonstrating that the assumption is not violated, based on the evidence available. If the results obtained violate the assumptions, then the assumption is proven wrong. If they do not, then the assumption cannot be rejected, and is hence considered to remain valid.

### 3.1. Advanced Image Quality Control, Example With Meteosat Geostationary Imagers

The Meteosat First Generation (MFG) satellites started the first series of continuous imaging over Africa and Europe (e.g., De Jong, 1978). The resulting images brought about new understanding of the weather patterns, but also uncovered a number of challenges for image processing that were unforeseen when the instruments were designed. The analysis of the resulting data record is impacted by so-called “image anomalies” (IA), which, for example, lead to under- or over-estimation of the radiance at the scene. This term is to be understood distinctly from its climate counterpart, where an anomaly is defined as the difference of a quantity with respect to some climatology. In the case of instrument operations, IA refers to an unexpected behavior that would cause improper interpretation of the image. As there is no reason to expect that such effects should cancel out, it is important to identify data affected by instrument issues, to avoid introducing spurious signals into long-term series. Several IA issues were not foreseen when the MVIRI instrument was initially designed. Methodologies to detect geostationary IA were developed over the years (e.g., Liefhebber et al., 2020) and cover a wide range of situations, from simple cases of complete image data corruption to more complex situations of regional over-illumination.

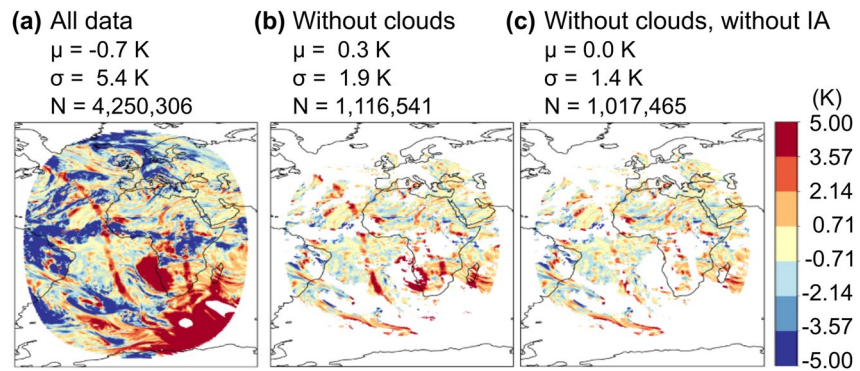


**Figure 1.** Maps of differences (in K) between observations and radiative transfer simulations using ERA5 for Meteosat-5 Meteosat Visible Infra-Red Imager water vapor channel, 16 October 1996 00 UTC: (a) all data, (b) results after excluding scenes believed to be cloudy, and (c) results after excluding in addition the scenes affected by image anomaly. Overall statistics ( $\mu$ ,  $\sigma$ ) and number of data (N) are reported at the top.

If occurrences of IA are correctly detected, masking out affected areas or images should lead to an improved agreement between images and other sources of information, such as radiative transfer from simulations. We verify this here in Figure 1 for a randomly picked date (16 October 1996) among dates when images anomalies were detected, from the MFG data record of Meteosat-5. Figure 1a shows a map of all the departures before any cloud or IA filtering. Figure 1b shows the results after applying a cloud mask (Stöckli et al., 2019). It can be seen that cloud masking improves the agreement between observations and simulations significantly, by reducing the standard deviation of differences over the full image from 5.4 to 1.9 K and by bringing the mean of differences closer to zero, from  $-0.7$  to 0.3 K. Figure 1c shows the results after filtering out scenes affected by an IA. In this case, the IA filtered out is direct stray light and over-illumination as defined by Liefhebber et al. (2020). The results indicate that this reduces the data count over the entire image by around 10%, but the agreement between observations and simulations is improved, with a standard deviation of differences reduced from 1.9 to 1.4 K, and a mean reduced to near-zero.

In summary, the radiative transfer simulations help us validate the assumption that an advanced image quality control should improve exploitation of the MVIRI data record.

### 3.2. Cloud Mask, Example With HIRS and AVHRR

An important objective of the assessment of the quality of satellite data records is to determine the quality of representation of climate time-scales. Such decadal products are of interest to users to study possibly small-scale variations over a long timeframe. There is a wide body of literature on data assessment (e.g., National Research Council (U.S.), 2004). However, from infra-red sounders and imagers, most retrievals schemes are restricted to clear-scenes only. For this reason, cloud mask validation is important.

Such activities are already performed routinely by cloud mask data producers. We show an example of how radiative transfer simulations can further assist in this fashion. To this end, we consider the infra-red and visible data records of two polar-orbiting instruments, the AVHRR and HIRS instruments, operated both on NOAA and EUMETSAT polar-orbiting satellites, and compare with clear-sky radiative transfer simulations.

The effects of clouds and aerosols are not included in the radiative transfer simulations considered here. Consequently, a large disagreement is expected around and after the time of the volcanic eruptions that generated considerable amounts of aerosols in the atmosphere. However, the effects of volcanic eruptions alone may not necessarily stand out because of other effects, such as spatial variability and clouds (ignored in the simulations). For this reason, we focus the evaluation on small geographical regions, to avoid potential issues of large-scale inhomogeneities within the region. The regions are as defined in the IPCC 6<sup>th</sup> Assessment Report (Iturbide et al., 2020).

Figure 2 shows, for the Equatorial Pacific Ocean region, the results of differences for the mode of differences (maximum of the departure distribution within a month) between observations and clear-sky radiative transfer simulations. The results are shown without any prior filtering for clouds. To obtain these timeseries, we first construct monthly histograms of departures, for each satellite and each channel, with a resolution of 0.1 K for brightness temperatures (HIRS and AVHRR infra-red channels) and of 0.1% for reflectance (AVHRR

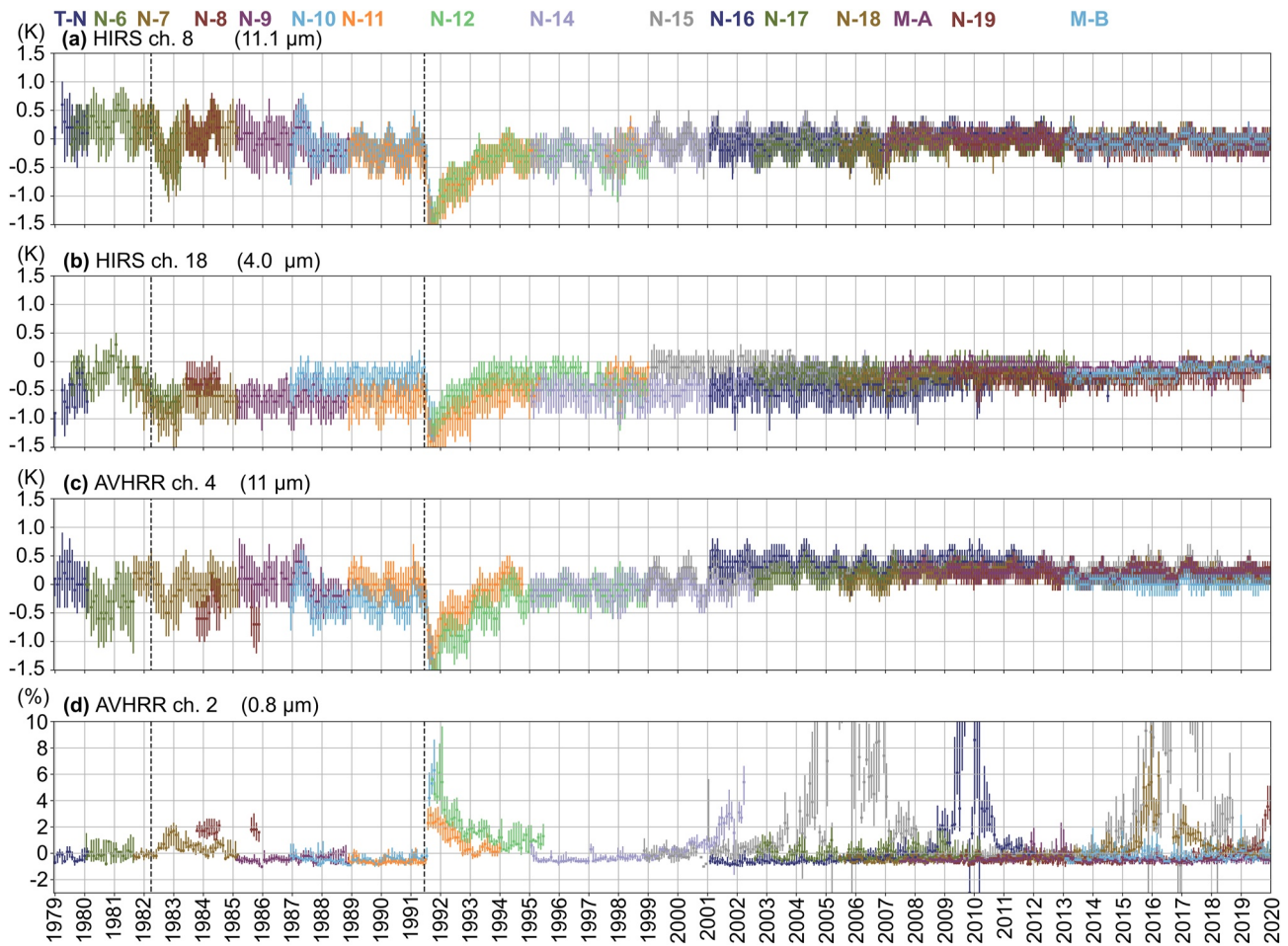


**Figure 2.** Monthly departures (modes as squares  $\pm$  vertical bars to indicate spread estimates, see text) between High-resolution Infrared Radiation Sounder, Advanced Very High Resolution Radiometer, and clear-sky radiative transfer simulations using ERA5, for the Equatorial Pacific Ocean region, between 1979 and 2020. Note two important volcanic eruptions: El Chichon (Mexico, 1982) and Mount Pinatubo (Philippines, 1991), with onsets indicated by vertical lines. Departures are shown for brightness temperatures (in K) for three infrared channels (a–c), and for reflectances (in %) for one visible channel (d). There is one color per satellite (from left to right, see top: T-N: TIROS-N, N-6 to N-19: NOAA-6 to –19, M-A and M-B: Metop-A and Metop-B).

near-infrared channel). For each histogram, we then estimate the mode of the distribution. Finally, we look on either side of the peak for values that delimit the 88% of the peak maximum. This allows us to quantify a peak width, which would approximate the standard deviation of departures if the distributions were normal. This metric is shown with bars around the mode.

We present here window channels, (respectively) HIRS channel 8 (thermal infrared at 11.1  $\mu\text{m}$ ), HIRS channel 18 (shortwave infrared at 4.0  $\mu\text{m}$ ), and AVHRR channel 4 (thermal infrared at 11.0  $\mu\text{m}$ ). For these channels, the departures generally feature negative biases, as expected, owing to the presence of clouds. Figures 2a–2c show the agreement between these observations and ERA5 improves from 1991 onwards, thanks to Sea-Surface Temperature information of high quality obtained from the well-calibrated sensors (Advanced) Along Track Scanning Radiometer ((A)ATSR) on European Remote Sensing satellites ERS-1/2 (and Envisat), as well as subsequent sensors, such as the Sea and Land Surface Temperature Radiometer (SLSTR) on Sentinel-3. For the AVHRR near-infrared channel 2, the departures in Figure 2d are generally within 0.5%, except for some satellite-dependent and volcanic eruptions episodes indicated by dashed vertical lines.

If the cloud mask is correct, we expect that its application would yield departures that are possibly closer to zero, depending on the reanalysis intrinsic biases, but also with a reduced standard deviation. Figure 3 shows this is indeed the case. Outside the volcanic eruption events, the standard deviations of departures (height of individual bars) are reduced from 0.6–0.8 to 0.4–0.6 K. The modes of departures for the HIRS channel 8 in Figure 3a feature a declining trend in the 1980s, not seen with the channels shown in Figures 3b and 3c. If the root cause of the

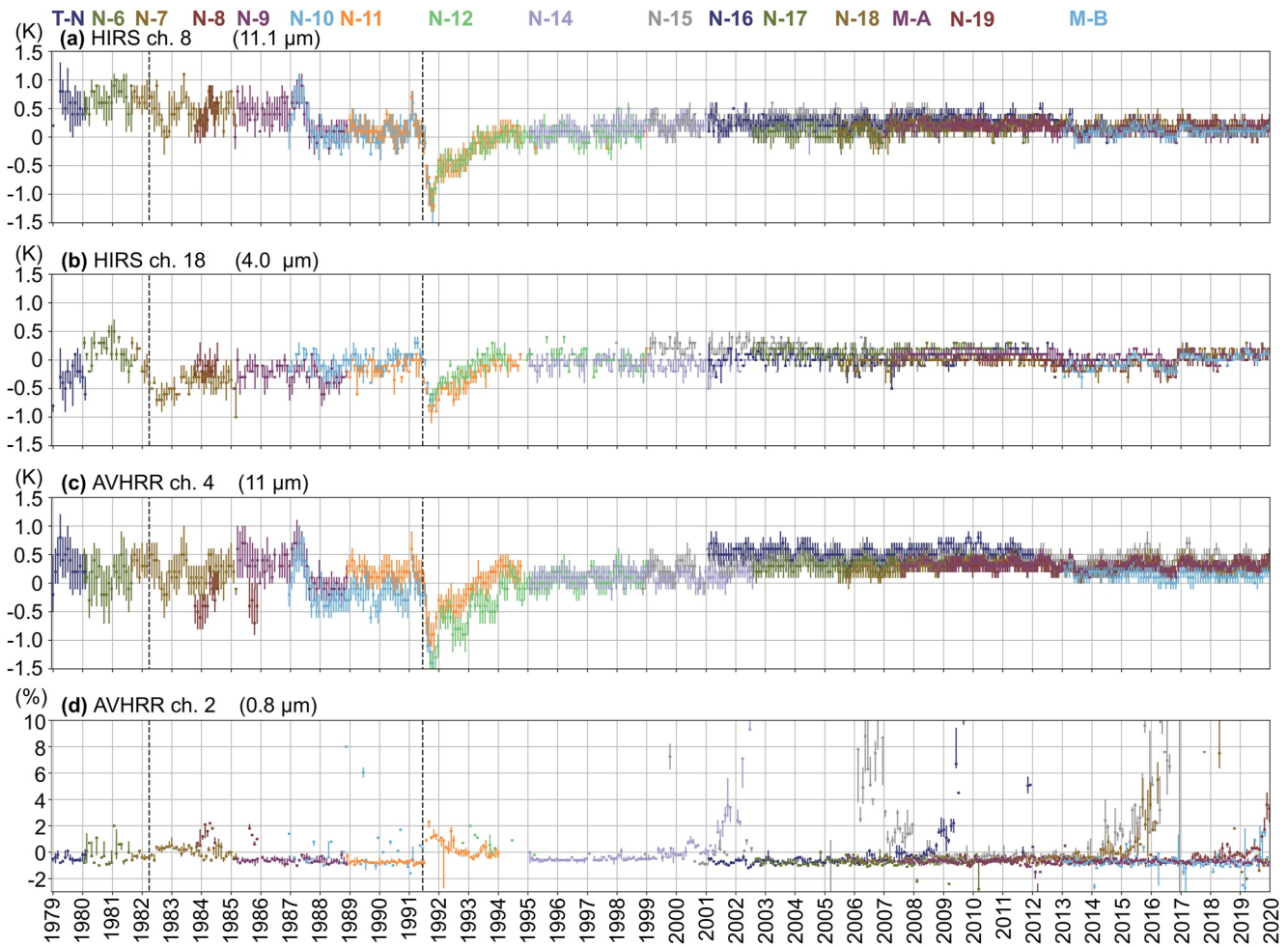


**Figure 3.** Similar to the previous figure, but restricting to scenes that are clear according to the cloud mask.

trend was only with a trend in biases in the reanalysis (ERA5) used for the simulations, then a similar behavior would show on the other channels, too, but it is not the case. This would suggest that the recalibration of HIRS channel 8 may benefit from further refinements. Note the effects of volcanic eruptions stand out in all timeseries.

The relevance of a cloud mask needing not to be demonstrated further, we now investigate the departures around the time of the Mount Pinatubo eruption in more details. The use of AVHRR to monitor volcanic ash is well-established (e.g., Watkin, 2003). For all the window channels, increased negative departures are observed in Figures 2 and 3 panels (a)–(c) around the time of the El Chichon and Pinatubo eruptions, as expected, with aerosols scattering radiation and emitting radiation from above the surface (hence at a colder temperature). For Pinatubo, the cooling anomaly in terms of brightness temperatures is on the order of 1 K, for short-wave and thermal channels alike, although the signatures differ somewhat between channels.

For the AVHRR near-infrared channel 2 (0.8  $\mu\text{m}$ ), reflectance departures are positive for 2–3 years after the event, between 2% and 5%, in Figure 2d. This is also as expected, due to scattering caused by the aerosols (and not simulated here). Unfortunately, the combination of rejection of high solar zenith angles with the selection of only clear scenes leads to discard most of the data for AVHRR channel 2, resulting in the prevalent absence of results for clear-scene reflectances in Figure 3d. We now turn to the spatial variability of this global event, by considering other IPCC regions.

Zooming in over a shorter time period (December 1990–January 1994), Figure 4 shows that the plume of aerosols took several months to propagate away from its origin in South-East Asia. Considering the minimum observed in departures by the infrared window channels (rows (a)–(c)), the effect of the eruption was most pronounced over the Tropical Indian Ocean 3 months after the eruption (column (i)), and then over the Tropical Pacific 4–5 months

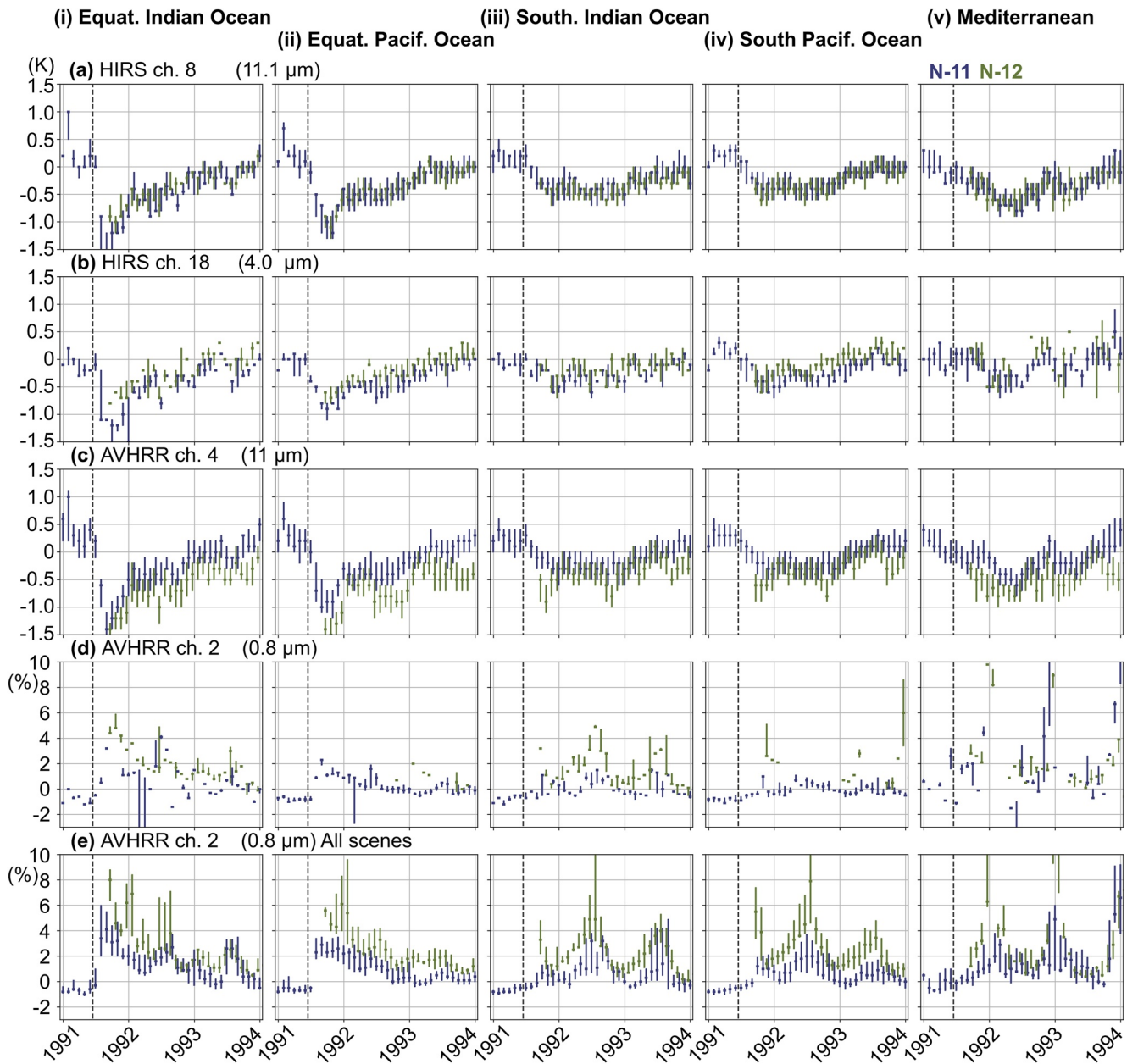


**Figure 4.** Similar to the previous figure, but showing several Intergovernmental Panel on Climate Change regions (see top, columns (i)–(v) from left to right) and zooming in on a time period starting 6 months before the Mount Pinatubo eruption (timing indicated by a vertical dotted line) and ending approximately 2.5 years after it. Note row (e) shows similar information as row (d) but for all scenes (i.e., without application of the cloud mask). There is one color per satellite (see top right, N-11 and N-12 for NOAA-11 and -12).

after the eruption (column (ii)), and again later in the southern latitudes (6–8 months, columns (iii), (iv)), with a further delay in the Mediterranean (up to a year, column (v)). Considering the maximum observed in reflectance departures by the near-infrared channel, the effect of the eruption was most pronounced over the Tropical Indian Ocean, and was felt in southern latitudes 2–3 months later, or in the Mediterranean 5–6 months later. The effects of this eruption were analyzed in detail previously (Stenchikov et al., 1998). However, the results shown here quantify the relevance of this episode with respect to the HIRS and AVHRR data records.

To summarize, this example validates the hypothesis that the CLARA-A3 cloud mask can help to (a) filter out cloudy scenes, and (b) quantify the radiative effects of the Mount Pinatubo eruption in the HIRS and AVHRR data records, with a separation between regional and temporal variations, at the wavelengths covered by the channels selected here.

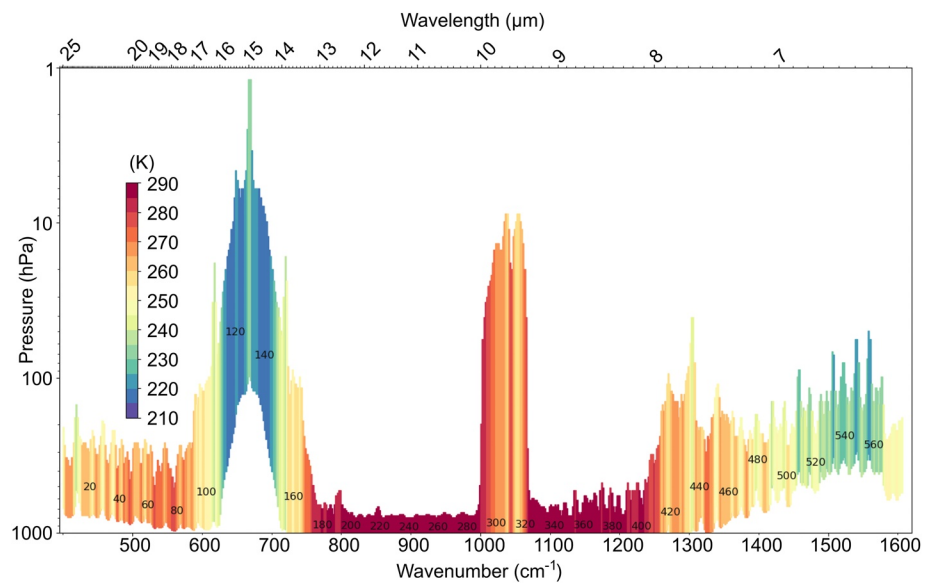


**Figure 5.** Spektrometer Interferometer wavelengths (top horizontal axis), wavenumbers (bottom horizontal axis), and RTTOV channel numbers (from left to right, in increments of 20). Each bar shows, horizontally, the nominal spectral resolution, and, vertically (bottom and top) the 5th to 95th percentiles (respectively) of the integrated weighting function, to help visualize where most of the atmospheric information comes from, for each channel, assuming clear-sky radiative transfer. Colors indicate the simulated brightness temperatures (in K, see scale). Calculations carried out from ERA5 data for a profile in the Spring over the Atlantic at the location (30°N, 30°W).

## 4. Class-II Applications: Assessing Coherence Between Reanalyses and Observations

### 4.1. Synoptic Timescales Coherence, Example With SI-1

The SI-1 instrument was a Michelson interferometer developed in the former German Democratic Republic, pursuing similar scientific objectives as the Infrared Interferometer Spectrometer (IRIS) instruments on-board Nimbus satellites covering the wavenumber range from 400 to 1,600  $\text{cm}^{-1}$  (Hanel et al., 1970, 1972). The first IRIS instrument was launched a few years earlier than the SI-1 instrument. More particularly, the SI-1 instrument was designed to allow identification of atmospheric constituents, clouds, as well as temperature sounding (Kempe, 1980; Kempe et al., 1980) as well as planetary exploration, as a similar instrument was deployed in the atmosphere of Venus (Oertel et al., 1985).

Most of the 579-channel data record from this instrument has been rescued by EUMETSAT (Théodore et al., 2015), and the comprehensive data record is being prepared for public data release with support from the European Union Copernicus Climate Change Service (C3S) at the time of writing. Figure 5 shows the spectral range covered by the instrument, and the vertical sensitivity of the channels to atmospheric information. The SI-1 instruments operated discontinuously in time and the resulting data record is too sparse to support consistent data assimilation in a global reanalysis. However, high-resolution spectral features are potentially useful to better understand subtle changes in the climate (e.g., Brindley & Bantges, 2016).

Another potential application of the SI-1 brightness temperatures is to use these to validate different reanalyses. We show an example here by considering a subset of the data record. Figures 6a and 6b shows the comparison of BT between observations and different reanalyses, for data at wavenumbers 400–1,200  $\text{cm}^{-1}$  collected by Meteor-29 over sea during the month of February 1979, for scenes to be believed free of clouds (123 spectra in total). The two panels separate between spectra that feature sharp departures (spikes) at wavenumbers 840–860 and 765–810  $\text{cm}^{-1}$ , across all reanalyses considered here. The reanalyses are ERA5, ERA-20C, JRA-55, and a preliminary version of the JRA-3Q reanalysis (a newer reanalysis as compared to JRA-55). For a fair comparison of the results, the ERA5 reanalysis profiles are considered every 6-hour, with a validity time window of  $\pm 3$  hours, like the other reanalyses (hourly ERA5 profiles at non-synoptic hours are ignored). The lower panels in Figure 6 show these departures. In a given column, the use of the same color across plots enables to appreciate that some degree of agreement exists sometimes between the reanalyses.

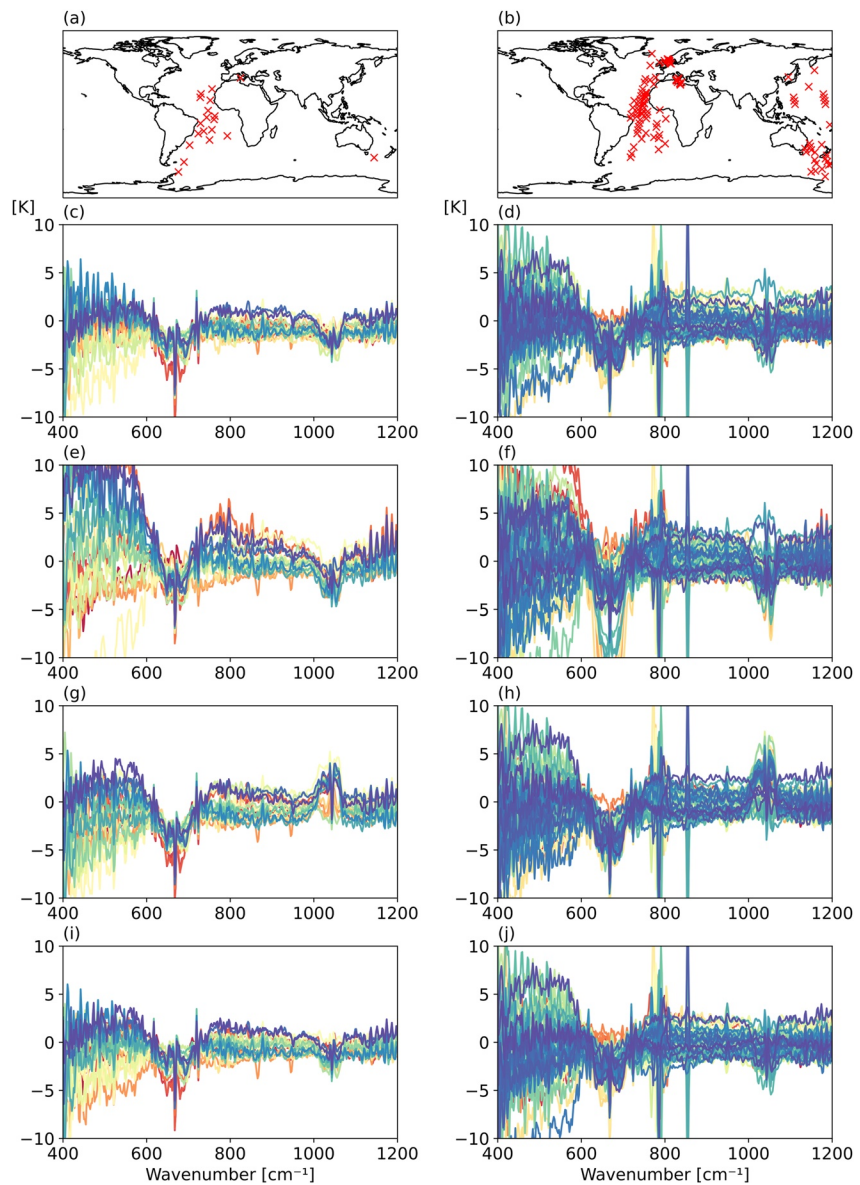


**Figure 6.** (a) Map of 19 Meteor-29 Spektrometer Interferometer (SI-1) observations in February 1979 without significant spectral spikes in regions 840–860 and 765–810  $\text{cm}^{-1}$ , and (b) map of 104 other Meteor-29 SI-1 observations presenting such spectral features. Bottom plots show corresponding differences in brightness temperature between observations and simulations, using (c, d) ERA5; (e, f) ERA-20C; (g, h) JRA-55; (i, j) a preliminary version of JRA-3Q.

Considering all the spectra shown in Figure 6, the Figure 7a shows mean differences between SI-1 brightness temperatures and the reanalyses. The standard deviations of departures are shown in Figure 7b. The dotted lines in Figures 7a–7b show statistics of brightness temperature (BT) departures between observations and simulations in radiance space, converted from difference radiance to equivalent difference BT at a nominal temperature of 280 K. Small differences with BT statistics are mostly visible where the brightness temperatures vary notably from this nominal temperature (see Figure 5), that is, for the top-peaking channels in the middle of the 1,041  $\text{cm}^{-1}$  ozone absorption line or 667  $\text{cm}^{-1}$   $\text{CO}_2$  absorption line, both sensitive to stratospheric temperatures. In this region, we find an agreement around 0.7–0.8 K in terms of equivalent difference BT (at 280 K) standard deviation.

Spikes are believed to be due to improper assumptions for trace gas concentrations in 1979 in our simulations. This is the case in particular near 845  $\text{cm}^{-1}$ , an absorption line of trichlorofluoromethane, also known as CFC-11 (e.g., J. J. Harrison, 2018). Similarly, a bulge in standard deviations is visible between 765 and 810  $\text{cm}^{-1}$ . Zenith

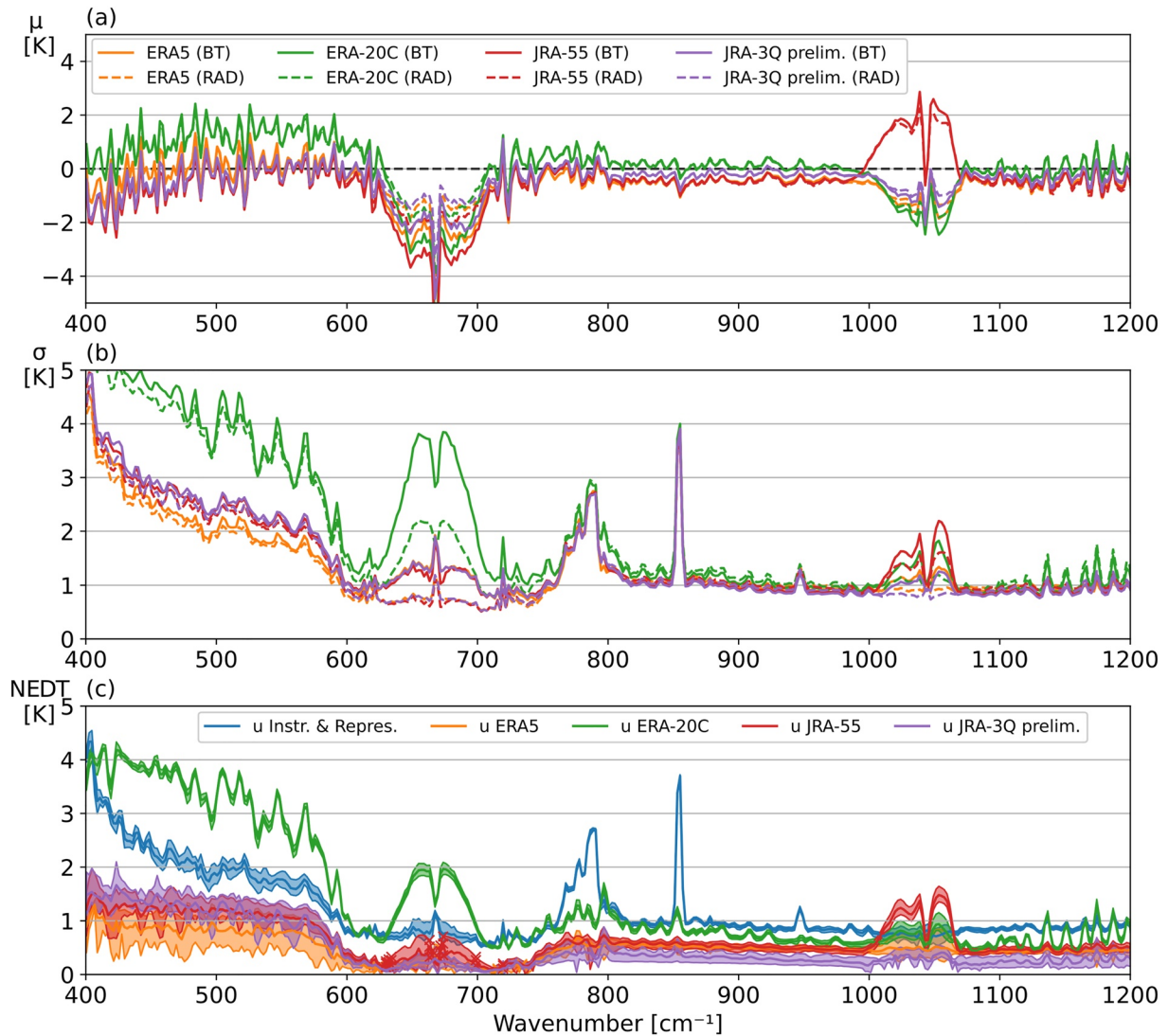


**Figure 7.** Departure (a) means ( $\mu$ ) and (b) standard deviations ( $\sigma$ ) of Brightness Temperature (BT) differences between 123 Meteor-29 SI-1 spectra shown in the previous figure and corresponding radiative transfer simulations using ERA5, ERA-20C, JRA-55, and a preliminary version of JRA-3Q (see legend). Dotted lines show similar statistics but based on radiance (RAD) differences, converted from difference radiance to difference BT at a nominal temperature of 280 K. Bottom plot (c) shows estimates of random uncertainties ( $u$ ), separating between each reanalysis random uncertainty, and combined observation and representativeness random uncertainty (see legend, and refer to text for details).

absorption spectra, such as reported in the Atmospheric Infrared Spectrum Atlas (King & Dudhia, 2017), indicate strong absorption features near  $775\text{ cm}^{-1}$  ( $\text{COF}_2$ ),  $780$  and  $810\text{ cm}^{-1}$  ( $\text{ClONO}_2$ ),  $785\text{ cm}^{-1}$  ( $\text{CClF}_3$ , also known as CFC-13),  $795\text{ cm}^{-1}$  ( $\text{CCl}_4$ ),  $810\text{ cm}^{-1}$  ( $\text{CHClF}_2$ , also known as HCFC-22), and  $780\text{--}805\text{ cm}^{-1}$  (peroxyacetyl nitrate,  $\text{CH}_3\text{C}(\text{O})\text{OONO}_2$ , also known as PAN). All these chemical constituents have seen large changes in concentrations over past decades owing to industrial emissions. Differences between present-day concentrations and those actually present in 1979 may be responsible for the departures reported here. Additional radiative transfer simulations, varying the absorber amounts, would help support investigations of such an hypothesis.

If the quality of JRA-3Q reanalysis improved as compared to the prior JRA-55 reanalysis, one would expect to see a better agreement with the simulations. The JRA-3Q improvements relative to JRA-55 in stratospheric ozone and stratospheric temperatures are clearly visible in Figures 7a and 7b around wavenumber  $1,041\text{ cm}^{-1}$  (sensitivity to stratospheric temperature and ozone) and wavenumber  $667\text{ cm}^{-1}$  (sensitivity to stratospheric temperature). The standard deviations of departures in the region  $600\text{--}700\text{ cm}^{-1}$  in Figure 7b also show that ERA-20C is an outlier, as compared to the other reanalyses, in terms of its fit to stratospheric-peaking channels located near the center of the line.

Having noticed in Figure 6 that spectral departures are sometimes similar across reanalyses, we apply similar concepts as those that underlie common uncertainty diagnostics (Desroziers et al., 2005). Assuming that all random uncertainties are independent from one another, we can estimate random uncertainties (see Text S2 in Supporting Information S1). Figure 7c shows the combined random uncertainties in the observations and radiative transfer (or representativeness), with a floor level in the range 0.8–1.0 K for most channels between 600 and 1,200  $\text{cm}^{-1}$ . We interpret spectral sharp departures above that floor level as deficiencies in the radiative transfer assumptions (e.g., incorrect absorber concentration, which yields departures that are correlated across all reanalyses, even though departures differ between different profile locations and dates and times).

Going from high to low wavenumbers, we observe an increase of the combined random uncertainties in the observations and radiative transfer (or representativeness). One may postulate that this increase is related to instrument noise. However, our random uncertainty estimation method does not separate between random instrument noise and random uncertainties in the radiative transfer model. Consequently, it could also be that the radiative transfer model is deficient in this region of the spectrum. There is indeed far less experience with observations of this far-infrared region of the spectrum than at wavenumbers in the range 650–1,600  $\text{cm}^{-1}$ . This situation should improve in future years with the Far-infrared Outgoing Radiation Understanding and Monitoring (FORUM) (Pachot et al., 2021). The FORUM instrument will indeed cover the spectral range between 100 and 1,600  $\text{cm}^{-1}$  (wavelengths between 6.2 and 100  $\mu\text{m}$ ) 0.3  $\text{cm}^{-1}$  of spectral sampling (5001 spectral elements).

Regarding the reanalyses, the estimates of random uncertainties are marked with crosses when the sum of squared uncertainties does not match the observed departure variance within a margin of 1% (this only occurs for some wavenumbers, in the region 620–750  $\text{cm}^{-1}$ ). Overall, we note that in most cases the findings agree with the considerations above, that is, the expectation that the ERA-20C reanalysis contains much less pertinent information in terms of thermal vertical structure than the other reanalyses shown here, and that JRA-3Q made significant improvements regarding stratospheric representation quality as compared to JRA-55.

An important caveat of our method is the assumption of independence of random uncertainties, that is, that cross-correlations between different uncertainty sources are zero. This may not be the case for a number of reasons, explained in the Text S2 in Supporting Information S1. In particular, the small spread between reanalyses may not reflect the true uncertainty but rather that these reanalyses share common uncertainties. For this reason, we believe that departures from this assumption are responsible for the very low level of random uncertainties (sometimes under 0.5 K) found for reanalyses. Conversely, some the uncertainties attributed to observations and radiative transfer (blue curve in Figure 7d) may actually come from uncertainties that are shared across the reanalyses, and hence may be over-estimated. Overall, we acknowledge that our method is not perfect but it still provides some initial insight into the uncertainties, which is a first for data collected by this early interferometer.

To summarize, this example illustrates how a high spectral resolution record, even when it is only short, can assist to measure progress in reanalyses.

#### 4.2. Understanding Differences via Bias Correction Linear Predictors, Example With MRIR

Bias correction methods aim at removing low-frequency variability in differences between observations and models, believed to be caused by systematic errors, for example, in the radiative transfer model or the instrument calibration (e.g., Dee & Uppala, 2009). In data assimilation, where radiance simulations are based on atmospheric profiles provided by a background, the methodology for such bias correction is now well-established. The bias is modeled as a linear combination of a set of predictors. Based on linear regression models, that is, one of many methods used in machine learning (e.g., Mitchell, 1997), bias corrections are thus effective tools to understand patterns of differences between observations and simulations.

For the infrared channels of the MRIR instrument, we investigate here the performance of extending the predictor set to include parameters believed to be at least in part related to instrument error. This analysis is restricted to daytime and ocean data only. Observations of the visible channel of MRIR are used to screen clouds, by excluding observations with an albedo greater than 0.1.

We compare the bias correction performances of three different bias predictor sets. The first predictor set is similar to that used in ERA-Interim and ERA5. This set includes four air mass predictors, in the form of geopotential layer thicknesses (1,000–300, 200–50, 10–1, and 50–5 hPa). One notes that corrections related to air mass are unlikely to be instrument-related, and may more closely relate to errors in the simulations (i.e., reanalysis in

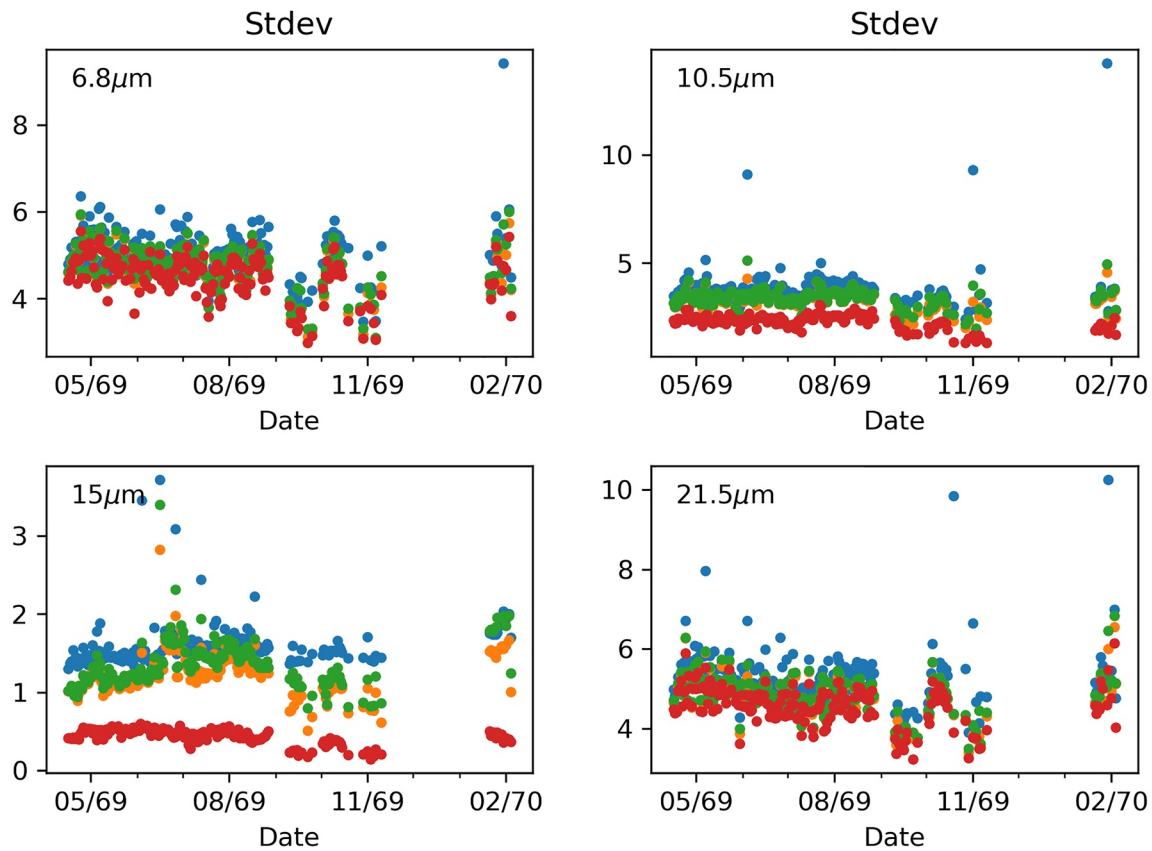


**Figure 8.** Time-series of daily Nimbus-3 (1969–1970) Medium-Resolution Infrared Radiometer departure standard deviations ( $\sigma$ , in K), for four different channels, without bias correction (blue dots), and with different bias correction schemes applied: ECMWF predictor set (orange dots), instrument predictor set (green dots) and combined predictor set (red dots). See text for details.

the present case). This predictor set also includes an offset, as well as the satellite viewing angle and its squared and cubed values. These four additional predictors are all expected to capture instrument and simulation errors, although noting the cubed value may capture foremost simulation errors. Note, the viewing angle is a parameter which may partly absorb calibration errors (e.g., Buehler et al., 2005).

The second predictor set is the so-called instrument predictor set. It excludes some of the predictors mentioned above that are believed to capture mostly simulation errors (layer thicknesses and satellite viewing angle cubed). However, it adds scene BT and instrument internal temperature. These two additional predictors are introduced to account for instrument errors due to uncertainties in gain and non-linearity effects, and instrument-temperature-related errors (respectively). Note, the scene BT is also expected to absorb some of the simulation errors.

Finally, the third predictor set considered combines all predictors of the first and second predictor sets.

Figure 8 shows the effects of applying the three bias predictor sets. The metric that is chosen for this assessment is the standard deviation of the Nimbus-3 MRIR departures ( $\sigma$ ). The mean departures, not shown, are reduced to near-zero in all cases, by design of the bias correction. The figure shows results without bias correction (blue), after applying the ECMWF predictor set (orange), the instrument predictor set (green), and the combined predictor set (red). As might be expected, all bias-corrected results fare better than the uncorrected case. In addition, the ECMWF and instrument predictor sets have similar impacts. The combined predictor set performs best of all. Especially for 10.5 and 15  $\mu\text{m}$  channels there are significant improvements to the standard deviations (note the factor two improvement for the 15  $\mu\text{m}$  channel). This indicates that both simulation and observation errors are significant. This also suggests that further studies of instrument-related departures should provide useful insights into the state of the instrument calibration.

In the case of the MRIR it is difficult to go beyond the bias correction models shown in Figure 8 as we lack the low level telemetry data (Level 0 data) that are needed to correct for instrument calibration errors at source.

In summary, this example shows that improvements may be made for MRIR to the bias correction models generally used in data assimilation, by considering likely instrument sources of uncertainties.

## 5. Class-III Applications: Informing Users

### 5.1. Unexplained Observation Variability, Example With SMMR

The microwave radiometer SMMR was a pioneering instrument for several fields in the Earth sciences. Two flight models were launched in 1978. The satellite carrying the first SMMR unit, Seasat, malfunctioned a few months after launch. The second SMMR unit, on Nimbus-7, operated for nearly 9 years, until August 1987. It offers an overlap, albeit limited, with the SSM/I (from July 1987). This particular time period is often looked at to enable inter-calibration of the two instruments' data records (e.g., Dai et al., 2015).

The SMMR instrument collected measurements at five microwave frequencies and two polarizations (vertical and horizontal). The complexities of this instrument and the resulting data record stem from the use of six radiometers to monitor 10 channels. This prevented continuous monitoring of all 10 channels for all footprints. Instead, the instrument used four radiometers to monitor the lower frequencies (6.6, 10.7, 18, and 21 GHz), by alternating polarization at each half-scan, while two other radiometers continuously monitored the 37 GHz frequency, at vertical and horizontal polarizations. However, most physical retrieval schemes were devised assuming data available from all channels. For this reason, the data processing includes a re-sampling of the data to cover all footprints.

NASA carried out the first and only full SMMR reprocessing within the Pathfinder project that was completed in the late 1990s (Njoku, 2003). This reprocessing included corrections for antenna pattern and polarization mixing. The reprocessing also revisited important components of the processing and applied lessons learned from the mission. This effort also unveiled new elements to address, such as a sharp change in Nimbus-7 spacecraft attitude in 1984, unaccounted for in this first reprocessing, as this issue was detected afterward.

The CM-SAF (Fennig et al., 2017) further attempted to reprocess the SMMR data. However, they could not start from the original low-level sensor data, as these data could not be located at the time. This means that several of the benefits expected from a full reprocessing could not be realized.

In this section, the reprocessed SMMR data from the CM-SAF are compared against radiative transfer simulations from two reanalyses, ERA-Interim and ERA5. Figure 9 shows that all frequencies present mean departures that are similar for ERA-Interim and ERA5, on the monthly timescales shown here, for the horizontal polarization. The data counts differ from ERA-Interim and ERA5 as approximately 4 times more data are being assessed in the case of ERA5 (hourly) than in the case of ERA-Interim (six-hourly).

Over oceans, SMMR data with rainy situations are excluded by checking distributions of departures (heuristic approach). Observations are considered rainy if the difference between horizontally polarized channels 37 GHz minus 18 GHz is outside the range (30 K, 50 K), if the difference between horizontally polarized channels 6.6 GHz minus 10.7 GHz is outside the range (−15 K, −5 K), if the polarization difference (vertical minus horizontal) at 37 GHz is less than 35 K, or if the BT at 18 GHz (6.6 GHz), horizontal polarization, exceeds 160 K (95 K, respectively). Data over land are not further analyzed here.

Figure 9d indicates spurious oscillations in the mean departures with respect to both reanalyses, before the 21 GHz radiometer (channel 9) failed in 1985. The magnitude of these oscillations grows over time, as well as the standard deviations of departures. Until such a behavior can be explained, these features can be interpreted as symptoms of a degradation over time of the horizontally-polarized 21 GHz channel.

During a Special Operations Period (SOP) that lasted from 3 April to 6 June 1986, the SMMR instrument was operated in a different mode. Instead of functioning every other day, the instrument was switched on and off more frequently, up to several times per day. The statistics indicate that it took some time after the SOP for the instrument to recover to its pre-SOP status. The exact cause for this behavior is unknown, but is suspected to be related to the SOP. The observed degradation is reported by Njoku (2003) to have lasted “during and for some time after the Special Operations Period.” This element is apparent for all channels as shown in Figure 9. The difference in statistics before and after the SOP is indeed evident for most channels shown. This points to a change in the calibration performance of the instrument after the 1986 SOP. In other terms, the data collected in 1987 may not be taken as representative of the instrument performance beforehand. Yet, the data from 1987 remain important as they are compared with SSM/I in order to inter-calibrate both records, as indicated above.

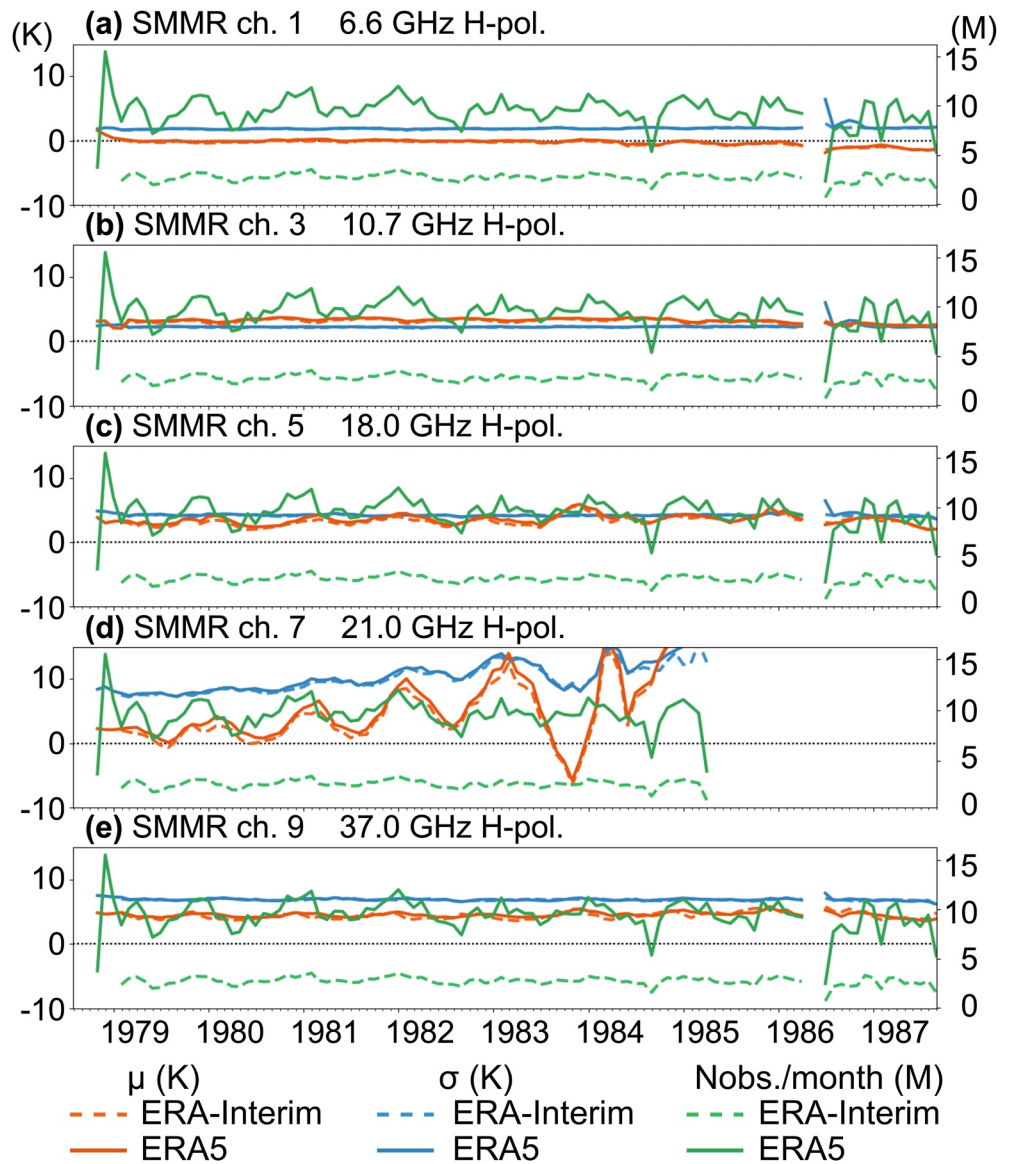


**Figure 9.** Time-series of monthly mean departures ( $\mu$ , orange) and standard deviations ( $\sigma$ , blue) between Scanning Multichannel Microwave Radiometer brightness temperatures and simulations using 6-hourly ERA-Interim and hourly ERA5 fields (see legend), for horizontally-polarized channels at frequencies (a) 6.6 GHz, (b) 10.7 GHz, (c) 18.0 GHz, (d) 21.0 GHz, and (e) 37.0 GHz, in K (left-hand-side vertical axis). The data counts per month (green) are reported (in millions, M) on the right-hand-side vertical axis.

To summarize, we find issues of channel performance degradation, large oscillating biases, and changes in calibration performance after the 1986 SOP. This information is potentially important information for users interested in climate applications. These issues are however difficult to address at the level of retrieval into geophysical quantities. This would rather need addressing with a new recalibration and reprocessing activity.

### 5.2. Explained Observation Variability, Example With MSG

The SEVIRI instruments on-board MSG satellites extend the data records started by MVIRI instruments on-board MFG satellites for the three heritage channels, that is, the water vapor, infrared, and visible channels. Furthermore, SEVIRI includes six additional channels in the infrared region as compared to MVIRI. When the MFG and MSG satellites are positioned near 0-degree longitude, the field of view of the instruments covers Africa and Europe. Thus, the observed radiances of these satellites allow patterns of variability to be inferred over areas with important societal applications (e.g., Barbosa et al., 2019; C. T. Harrison et al., 2019).

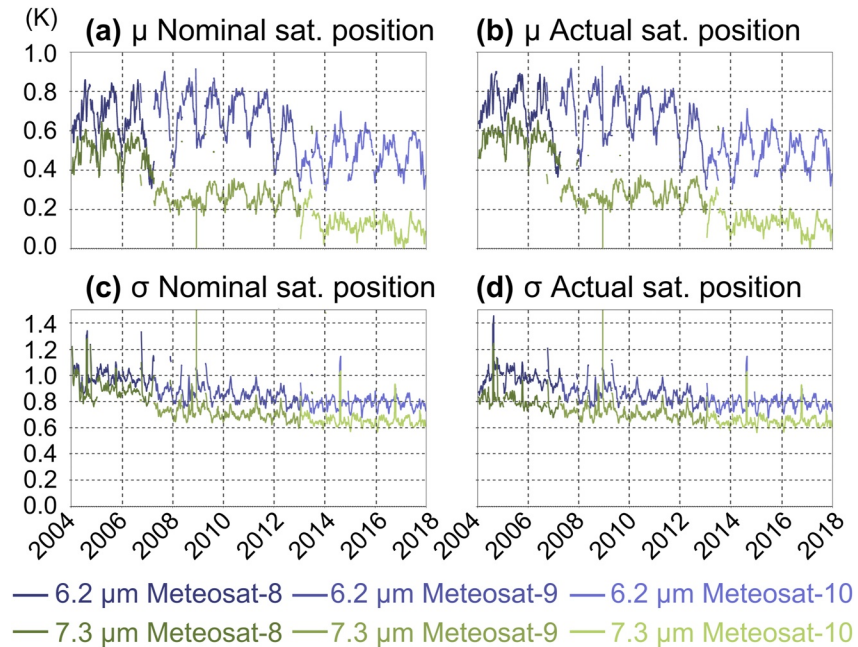


**Figure 10.** Time-series of (a, b) mean ( $\mu$ ) and (c, d) standard deviation ( $\sigma$ ) of departures for SEVIRI water vapor channels, using two different methods for the simulations: (a, c) assuming nominal satellite position at  $0^\circ$  longitude; (b, d) assuming the actual satellite position, as reported in the data.

Satellites in geostationary orbit are subject to small displacements around their nominal positions around the Equator. These satellites are affected by gravity pulls from the Earth and the Moon. This so called three-body system, or Lissajous track, results in figure-of-eight displacements (e.g., Hubert & Swale, 1984). In addition, geostationary satellites may see displacements during their lifetime when the nominal longitude changes. This section shows the importance for climate applications of these displacements (even if seemingly small), through an analysis of subsequent satellite data records that appear as originating from a single longitude position at the Equator.

The 15-min MSG All-Sky Radiances products are simulated here only for the two observation times closest to the hour (i.e., two images per hour are simulated, and two images are not). The quality controls applied selects only pixels that are believed to be free of clouds (so-called Clear-Sky Radiances, CSR), and for which the radiances are computed from an average of at least 10 pixels. These radiances are indeed horizontal averages of higher-resolution measurements.

The mean differences per month, as well as the standard deviations, between the MSG SEVIRI observations and the simulations based on ERA5, are shown for the whole observation area and for the two water vapor channels in Figure 10. In a first set of simulations, the nominal satellite position, at 0-degree longitude, is assumed. The resulting departures vary over time. Without any further indication to the contrary, a large part of these variations may be attributed to variations in the quality of the ERA5 reanalysis. In a second set of simulations, the radiative transfer simulations use as input the actual satellite position, as reported in the data, and thus can account for the effect of changing the viewing angle. This accounting has little impact on window channels (transparent to the atmosphere), but has some impact for channels measuring at the water vapor wavelengths. At these wavelengths the transmission is affected by the atmospheric optical depth. The comparison between Figures 10c and 10d indicates that the actual satellite position gives a slightly better agreement with the data record. However, the magnitude of the changes may appear negligible at first sight.

For this reason, it is important to investigate in more detail how these changes manifest themselves. To this end, we compute mean differences per month between the two sets of simulations, at a resolution of  $1^\circ \times 1^\circ$  latitude, longitude. This enables a Principal Component Analysis to be carried out, using the differences between the two simulations. Prior to this analysis, these differences are normalized to zero-mean and unit standard deviation for each given satellite and each given channel (e.g., Aires et al., 2002). Figure 11a indicates that the first eigenvectors

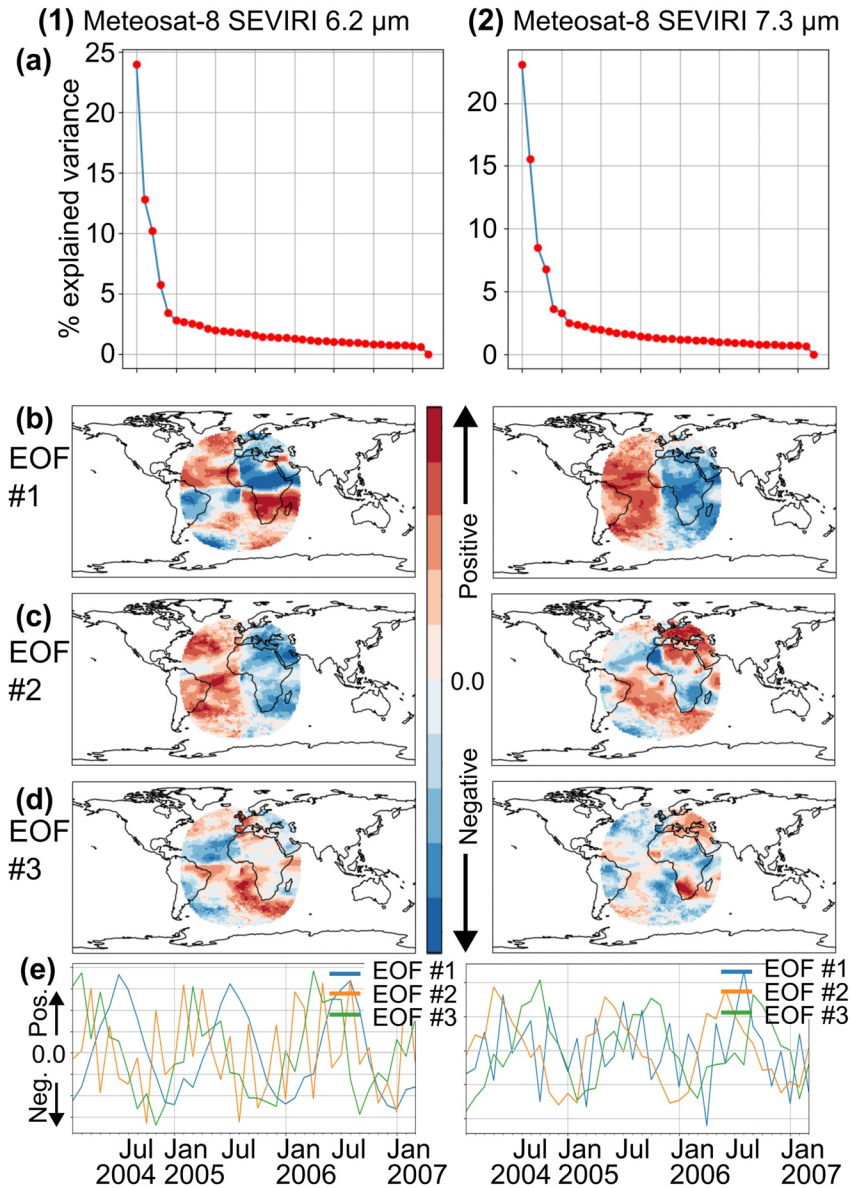


**Figure 11.** Results of Principal Component Analysis (PCA) analysis of normalized differences between radiative transfer simulations (assuming actual satellite position minus assuming nominal satellite position), for two water vapor channels indicated in columns (1) and (2), as follows: row (a) shows the percentage of explained variance by PCA EOF, rows (b)–(d) show the spatial projections of the first three EOFs, and row (e) shows these EOFs' time-varying amplitudes. Note that because of normalization the patterns of amplitudes are to be interpreted qualitatively in spatial terms or temporally (e.g., frequency and phase). To further avoid mis-interpretation into actual departures (in K) the normalized amplitudes of EOFs are shown without numerical axes.

(EOFs) explain most of the variability in the differences. The maps of these differences in Figures 11b–11d for the first three EOFs show the patterns of the differences. The temporal variations are also shown in Figure 11e, showing distinct cycles.

Because of the prior normalization of differences, the patterns evident in Figure 11 appear more important than they manifested in observation departure space analysis (in K) of Figure 10. These patterns present distinct spatial and temporal aspects that may easily be misinterpreted in terms of climate evolution terms, should they appear from an analysis of the observed geostationary radiance data after removal of other effects.

In summary, this example stresses the importance of correctly accounting for the satellite viewing angles when considering geostationary radiance data from water vapor channels, for climate applications. If this is not done,

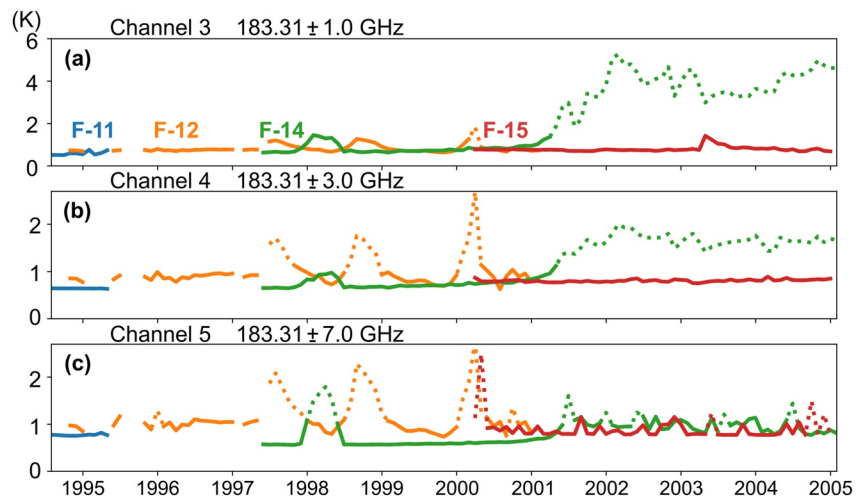


**Figure 12.** Total uncertainty (monthly mean) associated with the SSM/T-2 antenna temperatures, as a function of time, for the three 183.31 GHz channels, ordered from highest-peaking (a) to lowest-peaking (c), for all satellites (F-11, F-12, F-14, F-15, see colored labels). Dots indicate time periods excluded in subsequent data analysis because the uncertainty estimate exceeds twice the pre-launch noise equivalent delta temperature specification.

then erroneous signals will propagate into downstream applications, and get aliased into the findings, possibly affecting conclusions that may be drawn about regional patterns of changes.

### 5.3. Relevance of Uncertainty and Observation Horizontal Local Variability in a Data Record, Example With SSM/T-2

The SSM/T-2 microwave sounder data record was reprocessed by Hans et al. (2017), including estimates of uncertainty for the antenna temperatures. A later release of these reprocessed data included a cloud and rain mask (EUMETSAT, 2021), as these phenomena are known to hamper the ability to use the 183 GHz data for water vapor retrieval. The analysis presented in this section focuses on these channels.

The Quality Evaluation Report associated with the SSM/T-2 data record (EUMETSAT, 2021) shows that data present a few episodes of larger noise, most notably for the F-14 satellite after 2001. This total uncertainty information is shown in Figure 12. Using this information, episodes of increased noise may be removed by excluding all observations where the average total uncertainty exceeds twice the pre-launch noise equivalent delta temperature (NEDT) specifications of the given channel. The time periods that are removed by this procedure are shown in the same figure.

Hereafter we show that the uncertainty information helps to pinpoint other effects in the data. To this end, we consider the observation horizontal local variability ( $\Delta$ ), computed as the standard deviation of the observations over a  $3 \times 3$  horizontal array of neighboring pixels. We further restrict our analysis to latitudes between  $40^\circ\text{S}$  and  $40^\circ\text{N}$ . This is to ensure the data large-scale variability is driven by water vapor content and not by surface-induced emissivity, which may be more poorly simulated in some situations, for example, over sea-ice. We then bin all the results according to the observation horizontal local variability ( $\Delta$ ), in bins of 0.1 K. For each bin, we compute the data distribution (number of results found), as well as the mean and standard deviation of departures. The results are shown in Figure 13. The peaks in the data distributions indicate that the instruments have comparable noise characteristics. These peaks are situated in the region of 0.6–0.8 K, which is in line with the instrument NEDT specifications. The gradual increase in standard deviations as a function of observation horizontal local variability is also to be expected.

The mean departures in Figure 13a–c are not all aligned with each other, but present some (steady) offsets, depending on the satellites. This is most probably caused by the fact that Antenna Pattern Corrections were unknown and thus were not applied during the reprocessing. An alternative explanation for these offsets could be varying amounts of humidity biases (over time) in the ERA5 reanalysis. Such small inter-satellite differences are not believed to be a problem for applications of the SSM/T-2 data into reanalysis, which generally applies

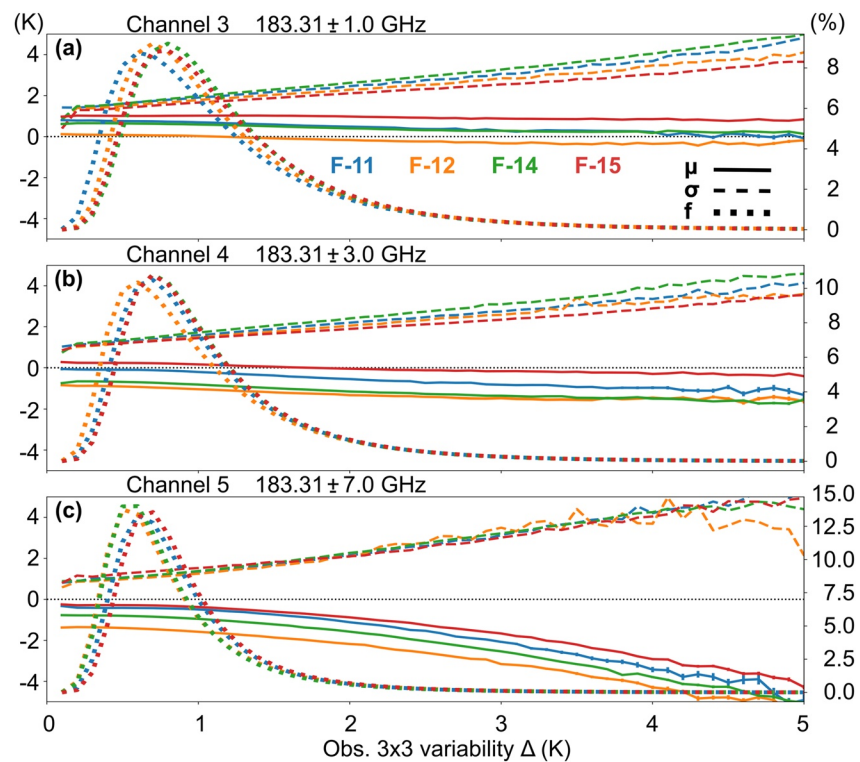


**Figure 13.** For the three SSM/T-2 183.31 GHz channels, (a)–(c), mean ( $\mu$ , solid lines) and standard deviation ( $\sigma$ , dashed lines) of departures (in K, left-hand-side vertical axis), as a function of the observation horizontal local variability ( $\Delta$ , horizontal axis, in bins of 0.1 K), with dotted lines showing the data distribution ( $f$ , normalized in percent, right-hand-side vertical axis).

bias corrections to such data when assimilating them. However, this does require further attention, to enable, for example, direct use of the data to retrieve humidity information, unless applying a priori approaches such as harmonization (e.g., Giering et al., 2019).

Finally, Figure 13 shows that the increase in observation horizontal local variability is associated with a slow but steady decrease of the bias toward negative values in the departures. This effect is most pronounced for the lowest-peaking channel in Figure 13c, and consistent with the findings of Calbet et al. (2018).

In summary, our simulation results indicate that the information about uncertainty and observation horizontal local variability should be of interest for users of the SSM/T-2 data interested, for example, in clear-sky humidity retrievals.

## 6. Discussion

There are several factors that could explain the departures between instrument data records and simulations from reanalyses reported and analyzed in this paper.

First, there is the issue of data independence. One needs to assess, for each comparison, if the observational data record was assimilated in the reanalysis that is used for the simulations. The data of several data records used in this paper were independent (SI-1, SSM/T-2, MRIR). Other data were partly or indirectly used in the reanalysis. As for example, is the case for the MVIRI radiances, which were indirectly assimilated as another variable or derived product. The HIRS data, on the other hand, were fully assimilated. However, our analysis only considers the low-frequency variability of departures. This variability is known to remain distinct between reanalysis and the assimilated data, thanks to the mechanism of the variational bias correction, even if the possibility of aliasing the signals cannot be ruled out completely.

Second, there are changes in reanalysis quality over time. These may be due to general improvement of the observing system (e.g., Dee et al., 2011), or related to instances of degraded performance owing to suboptimal

data use or more challenging natural variability, insufficiently observed, or suboptimal data use. When such changes occur, they will affect all comparisons, to all sensors, making it easier to identify whether or not the problem stems from the reanalysis or the satellite data record.

Third, even if different reanalyses (such as ERA5 and ERA-Interim) are from different generations, they often used very similar observations input (especially in the early years). This limits the degree of independence between comparisons to several reanalyses. For this reason, global reanalyses from a wider diversity of producers should be selected in future work.

Fourth, there are instrument-induced effects that are not all understood or simulated. A few of these effects are listed by Fennig et al. (2017), for example, for the Nimbus-7 SMMR data record. These effects include unknown variations in the satellite zenith angle, errors in the satellite attitude control, potential errors in the underlying level 1B processing and, more generally, insufficient correction of instrument-induced effects (such as calibration, spill-over, and polarization mixing). These are all effects that are best addressed at the source, and for which the simulations can help quantifying the overall cumulated effects. Even in cases where instrument errors cannot be corrected at the source, such as the case of the MRIR data record, improvements in bias correction predictors will help in including early satellite data into either data assimilation systems, or at least in its use as a check on aspects of a reanalysis for periods with limited or no satellite data.

Fifth, the quality of radiance simulations to reproduce the variability in the observations is not equal for all channels/instruments. This originates in the spatio-temporal scale and magnitude of natural phenomena responsible for the variability, differing by instrument and channel, as compared to instrument and simulation resolutions and uncertainties. One may cite as an example MVIRI, an instrument whose IFOV (see Table 1) is much smaller than the horizontal resolution of global reanalyses. The simulation of the MVIRI infrared window channel generally performs better over ocean than land, but on the other hand, the simulation of the MVIRI water vapor channel features larger spreads in departures than those of the window channels, owing to the upper-air water vapor coarse-resolution and corresponding variability representation in the reanalyses. Another example is when a satellite data record contains signals that originate from changes not contained in the simulations, such as volcanic aerosols (AVHRR) or possible changes in trace gases whose concentrations have evolved due to industrial emissions (SI-1). All these cases can be summed up by the issue of representativeness uncertainty between observations and reanalysis.

Overall, the general approach followed here can be summarized by three principles: (a) “all else being equal, an improved reprocessing should lead to an improved fit of the observed data to simulations,” and so should also (b) an improved simulation setup, and (c) an improved reanalysis. While this work is not a proof of these principles, we note that we have not found examples to the contrary in our investigations. However, one must remember that, under special circumstances, the situation of two observations and simulations agreeing for the wrong reason cannot be ruled out (e.g., Joiner et al., 2004). To reduce the chances of such mishap, we emphasize that the comparisons as shown here should, as much as possible, draw on a large number of data samples.

Another important element to consider, when analyzing departures between observations and simulations, are the quality controls (Text S1 in Supporting Information S1). They may appear as trivial to some readers, but far less obvious to others. While it should normally suffice to read the documentation that accompanies every data record, and then to apply the quality flags suggested by the documentation after reading the data, our experience suggests that more should be done in the future to ease the application of quality flags. The aim should be to preserve the flexibility for expert users but also to guide less-expert users and leave less room to interpretation.

Finally, an issue encountered during the course of this work was that each CDR tends to adopt a data representation that is contemporary to the time of the mission, reflecting in general the data transmission constraints imposed by radio transmission bandwidth and digitization. This is no different to practices followed to disseminate in-situ observation data. However, if one priority is to improve inter-operability of data sets for comparisons and other applications, the multitude of data models to represent observations is a barrier to integration. Indeed, it requires, in each case, to adapt computer code. To circumvent this issue, initiatives have been proposed, to promote a single data model (e.g., Nativi et al., 2008). Such initiatives will greatly simplify the data integration and data comparisons, for example, with other observations or with models, possibly via simulations as shown here.

## 7. Conclusions

This paper applies radiance simulators to the Fundamental (Climate) Data Records (F(C)DRs) of several satellite instruments, using as input global climate reanalyses. While the methodology of radiance simulators is not new, we demonstrate that their application enables three classes of applications.

In the first class of applications, assumptions about a data record organization (order of channels), its quality, or data corrections, may be verified. For this, we mostly draw from examples where the data have been characterized long ago, such as the MVIRI and HIRS data records, and much progress has been made since then. We use examples where the methodological advance of reprocessing is on a level that benefits from a high-quality a priori comparison to validate the impact, such as identifying IA in geostationary images or improving the coherence between data records and reanalyses with modern cloud masks.

Regarding the volcanic eruption of Mount Pinatubo, we find a cooling on the order of 1 K for brightness temperatures from AVHRR and HIRS window channels (short-wave and long-wave alike), with concomitant increase in reflectance for the AVHRR near-infrared channel of a few percent. We also revisit how fast the atmospheric effects of the eruption propagated away from the Tropics. In line with previous findings, we confirm differences in the timing of peak radiative effects of several months between the Mediterranean and the Southern Oceans as compared to the Tropics, where the volcanic eruption had taken place.

In the second class of applications, coherence between global data sets of different natures can be assessed. The high spectral resolution data collected by the SI-1 instrument allows confirmation of improvements in the quality of the latest Japanese global reanalysis, JRA-3Q, for stratospheric ozone. Spectral spikes in departures, observed for all reanalyses, also suggest that several trace gases' (in particular halocarbons) concentrations assumed in the radiative transfer may differ from actual concentrations in 1979. Furthermore, we present first estimates of SI-1 random uncertainty, assuming independence of random uncertainty between the sources of error. Given such caveats, our findings suggest the combined instrument noise and radiative transfer random uncertainties increase in the far-infrared region. In this respect, observations from the future FORUM instrument will be useful to enhance general experience and understanding of the performance of radiative transfer models in the far-infrared. At higher wavenumbers (600–1,200  $\text{cm}^{-1}$ ), we find combined SI-1 instrument noise equivalent delta temperature (NEDT) and representativeness uncertainties at 280 K to be generally in the range 0.8–1.0 K.

Another example shown, with MRIR, illustrates how differences, which could be interpreted as incoherencies between reanalyses and observations, can be differently reduced numerically, depending on the set of bias predictors chosen. While this can minimize systematic differences, another importance of this approach is to gain understanding about the potential sources of errors in the satellite data. This ties the present study to a third class of applications: informing users on key characteristics of a data record.

In this third class of applications, we show cases of simulations of, and comparisons with, data records from SMMR, SSM/T-2, and Meteosat second-generation. For SMMR, the findings are that the existing data records suffer for the horizontally-polarized 21 GHz channel from large oscillating biases, and that all channels exhibit a different behavior after a Special Observing Period in 1986. Given the value of the SMMR data in bridging with the SSM/I data record, this calls to consider a potential new reprocessing of the SMMR data record from the original data.

For SSM/T-2, we find that uncertainty information and horizontal local variability in the observations make a large difference to improve the agreement between reanalysis and clear-sky simulations. This suggests that these parameters would need to be taken into account in applications, such as clear-sky humidity retrievals.

For MSG, we find that the variability of the satellite position around its nominal position has most likely left a signature in the data record. For climate applications, such changes in position are needed to take into account or else they may get aliased into regional patterns of changes in the downstream products.

For all cases of the third class of applications, the results do not constitute final conclusions, but, instead, provide information for users and applications to take into account.

In all the examples shown in the study, the effort consists in bringing all the sources of information into the same observation space (times, locations, instrument channel, and viewing geometry), after having applied quality controls following the data records' user documentation. Notwithstanding the particular issue posed by the

diversity of observation data models, this approach, if generalized and made more systematic, would aid tracking of progress in climate reanalyses and satellite CDRs alike. This would help to accelerate the delivery of high-quality CDRs to serve climate services. The prospects for such an activity are not identified specifically in the GCOS Implementation Plan (World Meteorological Organization (WMO) et al., 2022). However, this plan identifies an action to co-locate in-situ and satellite measurements. The present paper demonstrates that there may be great benefits in considering also state-of-the-art reanalyses in such co-locations.

The data records discussed in this paper are mostly limited to the representation of atmospheric phenomena and corresponding satellite observations. In parallel, today's Earth system models are developed to encompass more components, including anthropogenic effects. One may thus expect the same methods as presented here to be applicable to support the development of data records related to other observables that impact our environment, such as human activity and biodiversity. These two fields are of utmost importance, provided that physical methods are developed to relate these fields to satellite measurements via simulators. For both fields, there have already been key developments (e.g., Gao et al., 2015; Schweiger & Laliberté, 2022, respectively). The methods set forth in the present paper may serve to continue progress in these areas and to support advances in long data records and corresponding models that describe human activity and biodiversity.

Thirty years after the 1992 Earth Summit, it is worth remembering that its participants had identified three topics to be tackled within regular meetings of Conventions Of the Parties, that is, climate change, biodiversity collapse, and desertification. Today, these three topics appear to be on a collision course, notwithstanding increasing demands for resources from a growing world population. This calls for more urgent action to understand the inter-relations between all these application areas, through better exploitation of environmental measurements, models, and reanalyses, which integrate the most diverse sources of data for our environment.

### Data Availability Statement

The satellite datasets analyzed in this study are available as follows: MVIRI (EUMETSAT, 2020): [https://doi.org/10.15770/EUM\\_SEC\\_CLM\\_0009](https://doi.org/10.15770/EUM_SEC_CLM_0009), SEVIRI (EUMETSAT, 2015): [https://doi.org/10.15770/EUM\\_SEC\\_CLM\\_0008](https://doi.org/10.15770/EUM_SEC_CLM_0008), MRIR (McCulloch, 2014): <https://doi.org/10.5067/XTJ53AK84QRL>, SI-1 (Poli et al., 2023): <https://doi.org/10.5281/zenodo.7912742>, HIRS (EUMETSAT, 2022): [https://doi.org/10.15770/EUM\\_SEC\\_CLM\\_0026](https://doi.org/10.15770/EUM_SEC_CLM_0026), AVHRR (EUMETSAT, 2023): [https://doi.org/10.15770/EUM\\_SEC\\_CLM\\_0060](https://doi.org/10.15770/EUM_SEC_CLM_0060), SMMR (Fennig et al., 2017): [https://doi.org/10.5676/EUM\\_SAF\\_CM/FCDR\\_MWI/V003](https://doi.org/10.5676/EUM_SAF_CM/FCDR_MWI/V003), SSM/T-2 (EUMETSAT, 2021): [https://doi.org/10.15770/EUM\\_SEC\\_CLM\\_0050](https://doi.org/10.15770/EUM_SEC_CLM_0050), and CLARA-A3 cloud mask (Karlsson et al., 2023): [https://doi.org/10.5676/EUM\\_SAF\\_CM/CLARA\\_AVHRR/V003](https://doi.org/10.5676/EUM_SAF_CM/CLARA_AVHRR/V003). The reanalysis datasets are available as follows: ERA5 (Copernicus Climate Change Service, 2018): <https://doi.org/10.24381/cds.bd0915c6>, ERA-20C (ECMWF, 2014): <https://doi.org/10.5065/D6VQ30QG>, ERA-Interim (ECMWF, 2009): <https://doi.org/10.5065/D6CR5RD9>, JRA-55 (Japan Meteorological Agency, 2013): <https://search.diasjp.net/en/dataset/JRA55>, and JRA-3Q (Japan Meteorological Agency, 2022): <https://search.diasjp.net/en/dataset/JRA3Q>. The radiance simulator used in this study is RADSIM (EUMETSAT NWP-SAF, 2021), available from <https://nwp-saf.eumetsat.int/site/software/radiance-simulator/>. We used RADSIM version 3.0. The radiative transfer model used in this study is RTTOV (EUMETSAT NWP-SAF, 2020), available from: <https://nwp-saf.eumetsat.int/site/software/rttov/>. We used RTTOV version v13.0 except for simulating MRIR, where RTTOV v12.2 was used.

### Acknowledgments

This work benefited from strong inter-agency collaboration, noting support from the European Union Copernicus Climate Change Service (C3S) and the institutions to which the authors are affiliated. The EUMETSAT NWP-SAF is thanked for adding support to several instruments, with special thanks to Emma Turner and James Hocking. The EUMETSAT CM-SAF is acknowledged for providing data records used in this work, and special thanks are addressed to Karl-Göran Karlsson, Abhay Devasthale, Martin Raspaud, Diana Stein, Nathalie Selbach, Stephan Finkensieper, Karsten Fennig, Marc Schröder, and Rainer Hollmann. The authors wish to thank NOAA for the SSM/T-2 Sensor Data Record. The authors also wish to thank librarians at EUMETSAT, NASA, and NOAA for help locating early satellite instruments' technical documentation.

### References

- Aires, F., Rossow, W. B., & Chédin, A. (2002). Rotation of EOFs by the independent component analysis: Toward a solution of the mixing problem in the decomposition of geophysical time series. *Journal of the Atmospheric Sciences*, 59(1), 111–123. [https://doi.org/10.1175/1520-0469\(2002\)059<0111:ROEBTI>2.0.CO;2](https://doi.org/10.1175/1520-0469(2002)059<0111:ROEBTI>2.0.CO;2)
- Andersson, A., Graw, K., Schröder, M., Fennig, K., Liman, J., Bakan, S., et al. (2017). *Hamburg Ocean atmosphere parameters and fluxes from satellite data—HOAPS 4.0 [NetCDF v4]*. Satellite Application Facility on Climate Monitoring (CM SAF). [https://doi.org/10.5676/EUM\\_SAF\\_CM/HOAPS/V002](https://doi.org/10.5676/EUM_SAF_CM/HOAPS/V002)
- Barbosa, H. A., Lakshmi Kumar, T. V., Paredes, F., Elliott, S., & Ayuga, J. G. (2019). Assessment of Caatinga response to drought using meteosat-SEVIRI normalized difference vegetation index (2008–2016). *ISPRS Journal of Photogrammetry and Remote Sensing*, 148, 235–252. <https://doi.org/10.1016/j.isprsjprs.2018.12.014>
- Bell, B., Hersbach, H., Simmons, A., Berrisford, P., Dahlgren, P., Horányi, A., et al. (2021). The ERA5 global reanalysis: Preliminary extension to 1950. *Quarterly Journal of the Royal Meteorological Society*, 147(741), 4186–4227. <https://doi.org/10.1002/qj.4174>
- Bell, W., Di Michele, S., Bauer, P., McNally, T., English, S. J., Atkinson, N., et al. (2010). The radiometric sensitivity requirements for satellite microwave temperature sounding instruments for numerical weather prediction. *Journal of Atmospheric and Oceanic Technology*, 27(3), 443–456. <https://doi.org/10.1175/2009JTECHA1293.1>

- Brasseur, G. P., & Gallardo, L. (2016). Climate services: Lessons learned and future prospects. *Earth's Future*, 4(3), 79–89. <https://doi.org/10.1002/2015EF000338>
- Brindley, H. E., & Bantges, R. J. (2016). The spectral signature of recent climate change. *Current Climate Change Reports*, 2(3), 112–126. <https://doi.org/10.1007/s40641-016-0039-5>
- Buehler, S. A., Kuvатов, M., & John, V. O. (2005). Scan asymmetries in AMSU-B data. *Geophysical Research Letters*, 32(24), L24810. <https://doi.org/10.1029/2005GL024747>
- Calbet, X., Peinado-Galan, N., DeSouza-Machado, S., Kursinski, E. R., Oria, P., Ward, D., et al. (2018). Can turbulence within the field of view cause significant biases in radiative transfer modeling at the 183 GHz band? *Atmospheric Measurement Techniques*, 11(12), 6409–6417. <https://doi.org/10.5194/amt-11-6409-2018>
- Copernicus Climate Change Service. (2018). ERA5 [Dataset]. Copernicus Climate Change Service (C3S) Data Store. <https://doi.org/10.24381/cds.bd0915c6>
- Dai, L., Che, T., & Ding, Y. (2015). Inter-calibrating SMMR, SSM/I and SSMI/S data to improve the consistency of snow-depth products in China. *Remote Sensing*, 7(6), 7212–7230. <https://doi.org/10.3390/rs70607212>
- Dee, D. P., Uppala, S. M., Simmons, A. J., Berrisford, P., Poli, P., Kobayashi, S., et al. (2011). The ERA-interim reanalysis: Configuration and performance of the data assimilation system. *Quarterly Journal of the Royal Meteorological Society*, 137(656), 553–597. <https://doi.org/10.1002/qj.828>
- Dee, D. P., & Uppala, S. (2009). Variational bias correction of satellite radiance data in the ERA-Interim reanalysis. *Quarterly Journal of the Royal Meteorological Society*, 135(644), 1830–1841. <https://doi.org/10.1002/qj.493>
- De Jong, E. (1978). Space age computing. *Physics Bulletin*, 29(10), 459–462. <https://doi.org/10.1088/0031-9112/29/10/017>
- Desroziers, G., Berre, L., Chapnik, B., & Poli, P. (2005). Diagnosis of observation, background and analysis-error statistics in observation space. *Quarterly Journal of the Royal Meteorological Society*, 131(613), 3385–3396. <https://doi.org/10.1256/qj.05.108>
- De Vrese, P., & Hagemann, S. (2018). Uncertainties in modelling the climate impact of irrigation. *Climate Dynamics*, 51(5–6), 2023–2038. <https://doi.org/10.1007/s00382-017-3996-z>
- Doutriaux-Boucher, M., Pelon, J., Trouillet, V., Sèze, G., Le Treut, H., Flamant, P., & Desbois, M. (1998). Simulation of satellite lidar and radiometer retrievals of a general circulation model three-dimensional cloud data set. *Journal of Geophysical Research*, 103(D20), 26025–26039. <https://doi.org/10.1029/98JD02378>
- ECMWF. (2009). ERA-Interim [Dataset]. UCAR/NCAR—Research Data Archive. <https://doi.org/10.5065/D6CR5RD9>
- ECMWF. (2014). ERA-20C project: ECMWF atmospheric reanalysis of the 20th century [Dataset]. UCAR/NCAR—Research Data Archive. <https://doi.org/10.5065/D6VQ30QG>
- EUMETSAT. (2015). All-sky radiances—MSG—0 degree (CF-015 release 1) [Dataset]. European Organisation for the Exploitation of Meteorological Satellites Data Store. [https://doi.org/10.15770/EUM\\_SEC\\_CLM\\_0008](https://doi.org/10.15770/EUM_SEC_CLM_0008)
- EUMETSAT. (2020). MVIRI level 1.5 climate data record release 1—MFG—0 degree [Dataset]. European Organisation for the Exploitation of Meteorological Satellites Data Store. [https://doi.org/10.15770/EUM\\_SEC\\_CLM\\_0009](https://doi.org/10.15770/EUM_SEC_CLM_0009)
- EUMETSAT. (2021). SSM/T-2 microwave humidity sounder climate data record release 2—DMSP (version 2) [Dataset]. European Organisation for the Exploitation of Meteorological Satellites Data Store. [https://doi.org/10.15770/EUM\\_SEC\\_CLM\\_000910.15770/EUM\\_SEC\\_CLM\\_0050](https://doi.org/10.15770/EUM_SEC_CLM_000910.15770/EUM_SEC_CLM_0050)
- EUMETSAT. (2022). HIRS level 1C fundamental data record release 1—multimission-global [Dataset]. European Organisation for the Exploitation of Meteorological Satellites Data Store. [https://doi.org/10.15770/EUM\\_SEC\\_CLM\\_0026](https://doi.org/10.15770/EUM_SEC_CLM_0026)
- EUMETSAT. (2023). AVHRR fundamental data record—Release 1—Multimission. [Dataset]. European Organisation for the Exploitation of Meteorological Satellites Data Store. [https://doi.org/10.15770/EUM\\_SEC\\_CLM\\_0060](https://doi.org/10.15770/EUM_SEC_CLM_0060)
- EUMETSAT NWP-SAF. (2020). Radiative transfer for TOVS (RTTOV). [Software]. (Version 13.0). Retrieved from <https://nwp-saf.eumetsat.int/site/software/rttov/download/>
- EUMETSAT NWP-SAF. (2021). Radiance simulator (RADSIM). [Software]. (Version 3.0). Retrieved from <https://nwp-saf.eumetsat.int/site/software/radiance-simulator/download/>
- Fennig, K., Schröder, M., & Hollmann, R. (2017). Fundamental climate data record of microwave imager radiances, edition 3 [Dataset]. Satellite Application Facility on Climate Monitoring (CM SAF). [https://doi.org/10.5676/EUM\\_SAF\\_CM/FCDR\\_MWI/V003](https://doi.org/10.5676/EUM_SAF_CM/FCDR_MWI/V003)
- Gao, B., Huang, Q., He, C., & Ma, Q. (2015). Dynamics of urbanization levels in China from 1992 to 2012: Perspective from DMSP/OLS nighttime light data. *Remote Sensing*, 7(2), 1721–1735. <https://doi.org/10.3390/rs70201721>
- Gibson, J., Källberg, P. W., Uppala, S., Hernandez, A., Nomura, A., & Serrano, E. (1997). *ERA description (ERA report No. 1)*. ECMWF. Retrieved from <https://www.ecmwf.int/en/eLibrary/74605-era-description>
- Giering, R., Quast, R., Mittaz, J. P. D., Hunt, S. E., Harris, P. M., Woolliams, E. R., & Merchant, C. J. (2019). A novel Framework to harmonise satellite data series for climate applications. *Remote Sensing*, 11(9), 1002. <https://doi.org/10.3390/rs11091002>
- Gordon, A. H. (1962). Satellite meteorology. *Nature*, 195(4847), 1161–1162. <https://doi.org/10.1038/1951161a0>
- Hanel, R. A., Conrath, B. J., Kunde, V. G., Prabhakara, C., Revah, I., Salomonson, V. V., & Wolford, G. (1972). The Nimbus 4 infrared spectroscopy experiment: 1. Calibrated thermal emission spectra. *Journal of Geophysical Research*, 77(15), 2629–2641. <https://doi.org/10.1029/JC077i015p02629>
- Hanel, R. A., Schlachman, B., Clark, F. D., Prokesh, C. H., Taylor, J. B., Wilson, W. M., & Chaney, L. (1970). The Nimbus III Michelson interferometer. *Applied Optics*, 9(8), 1767. <https://doi.org/10.1364/AO.9.001767>
- Hans, I., Burgdorf, M., John, V. O., Mittaz, J., & Buehler, S. A. (2017). Noise performance of microwave humidity sounders over their lifetime. *Atmospheric Measurement Techniques*, 10(12), 4927–4945. <https://doi.org/10.5194/amt-10-4927-2017>
- Harrison, C. T., Washington, R., & Engelstaedter, S. (2019). A 14-year climatology of Saharan dust emission mechanisms inferred from automatically tracked plumes. *Journal of Geophysical Research: Atmospheres*, 124(16), 9665–9690. <https://doi.org/10.1029/2019JD030291>
- Harrison, J. J. (2018). New and improved infrared absorption cross sections for trichlorofluoromethane (CFC-11). *Atmospheric Measurement Techniques*, 11(10), 5827–5836. <https://doi.org/10.5194/amt-11-5827-2018>
- Hasselmann, K. (1997). Multi-pattern fingerprint method for detection and attribution of climate change. *Climate Dynamics*, 13(9), 601–611. <https://doi.org/10.1007/s003820050185>
- Hersbach, H., Bell, B., Berrisford, P., Hirahara, S., Horányi, A., Muñoz-Sabater, J., et al. (2020). The ERA5 global reanalysis. *Quarterly Journal of the Royal Meteorological Society*, 146(730), 1999–2049. <https://doi.org/10.1002/qj.3803>
- Hocking, J. (2022). *Radiance simulator v3.1 user guide (No. NWP/SAF-MO-UD-051)*. EUMETSAT NWP-SAF. Retrieved from [https://nwp-saf.eumetsat.int/site/download/documentation/rad\\_sim/user\\_documentation/RadSim\\_UserGuide.pdf](https://nwp-saf.eumetsat.int/site/download/documentation/rad_sim/user_documentation/RadSim_UserGuide.pdf)
- Houborg, R., & McCabe, M. F. (2016). Adapting a regularized canopy reflectance model (REGFLEC) for the retrieval challenges of dryland agricultural systems. *Remote Sensing of Environment*, 186, 105–120. <https://doi.org/10.1016/j.rse.2016.08.017>

- Hubert, S., & Swale, J. (1984). Station keeping of a constellation of geostationary communications satellites. In *Astrodynamics conference*. American Institute of Aeronautics and Astronautics. <https://doi.org/10.2514/6.1984-2042>
- Hunt, G. E., & Grant, I. P. (1969). Discrete space theory of radiative transfer and its application to problems in planetary atmospheres. *Journal of the Atmospheric Sciences*, 26(5), 963–972. [https://doi.org/10.1175/1520-0469\(1969\)026<0963:DSTORT>2.0.CO;2](https://doi.org/10.1175/1520-0469(1969)026<0963:DSTORT>2.0.CO;2)
- Turbide, M., Gutiérrez, J. M., Alves, L. M., Bedia, J., Cerezo-Mota, R., Cimadevilla, E., et al. (2020). An update of IPCC climate reference regions for subcontinental analysis of climate model data: Definition and aggregated datasets. *Earth System Science Data*, 12(4), 2959–2970. <https://doi.org/10.5194/essd-12-2959-2020>
- Jackson, D. L., & Soden, B. J. (2007). Detection and correction of diurnal sampling bias in HIRS/2 brightness temperatures. *Journal of Atmospheric and Oceanic Technology*, 24(8), 1425–1438. <https://doi.org/10.1175/JTECH2062.1>
- Japan Meteorological Agency. (2013). The Japanese 55-year reanalysis (JRA-55) [Dataset]. Japan Agency for Marine-Earth Science and Technology Data Integration and Analysis System (DIAS). Retrieved from <https://search.diasjp.net/en/dataset/JRA55>
- Japan Meteorological Agency. (2022). The Japanese reanalysis for three quarters of a century (JRA-3Q). [Dataset]. Japan Agency for Marine-Earth Science and Technology Data Integration and Analysis System (DIAS). Retrieved from <https://search.diasjp.net/en/dataset/JRA3Q>
- John, V. O., & Buehler, S. A. (2004). The impact of ozone lines on AMSU-B radiances. *Geophysical Research Letters*, 31(21), L21108. <https://doi.org/10.1029/2004GL021214>
- Joiner, J., & Poli, P. (2005). Note on the effect of horizontal gradients for nadir-viewing microwave and infrared sounders. *Quarterly Journal of the Royal Meteorological Society*, 131(608), 1783–1792. <https://doi.org/10.1256/qj.04.125>
- Joiner, J., Poli, P., Frank, D., & Liu, H. C. (2004). Detection of cloud-affected AIRS channels using an adjacent-pixel approach. *Quarterly Journal of the Royal Meteorological Society*, 130(599), 1469–1487. <https://doi.org/10.1256/qj.03.93>
- Joiner, J., & Rokke, L. (2000). Variational cloud-clearing with TOVS data. *Quarterly Journal of the Royal Meteorological Society*, 126(563), 725–748. <https://doi.org/10.1002/qj.49712656316>
- Karlsson, K.-G., Riihela, A., Trentmann, J., Stengel, M., Solodovnik, I., Meirink, J. F., et al. (2023). CLARA-A3: CM SAF cLoud, albedo and surface RAdiation dataset from AVHRR data—Edition 3 (version 3.0) [Dataset]. Satellite Application Facility on Climate Monitoring (CM SAF). [https://doi.org/10.5676/EUM\\_SAF\\_CM/CLARA\\_AVHRR/V003](https://doi.org/10.5676/EUM_SAF_CM/CLARA_AVHRR/V003)
- Kempe, V. (1980). Satellite-Fourier-spectrometer for meteor-25: Design problems and mission. *Acta Astronautica*, 7(7), 893–902. [https://doi.org/10.1016/0094-5765\(80\)90078-8](https://doi.org/10.1016/0094-5765(80)90078-8)
- Kempe, V., Oertel, D., Schuster, R., Becker-Ross, H., & Jahn, H. (1980). Absolute IR-spectra from the measurement of Fourier-spectrometers aboard Meteor 25 and 28. *Acta Astronautica*, 7(12), 1403–1416. [https://doi.org/10.1016/0094-5765\(80\)90015-6](https://doi.org/10.1016/0094-5765(80)90015-6)
- King, O., & Dudhia, A. (2017). Atmospheric infrared spectrum atlas: Zenith sky optical thickness infrared spectrum. Retrieved from <http://eodg.atm.ox.ac.uk/ATLAS/zenith-absorption>
- Kobayashi, S., Kosaka, Y., Chiba, J., Tokuhiro, T., Harada, Y., Kobayashi, C., & Naoe, H. (2021). JRA-3Q: Japanese reanalysis for three quarters of a century. In *Presented at the joint WCRP-WWRP symposium on data assimilation and reanalysis/ECMWF annual seminar 2021, online*. Retrieved from <https://symp-bonn2021.sciencesconf.org/data/355900.pdf>
- Kobayashi, S., Ota, Y., Harada, Y., Ebata, A., Moriya, M., Onoda, H., et al. (2015). The JRA-55 reanalysis: General specifications and basic characteristics. *Journal of the Meteorological Society of Japan. Ser. II*, 93(1), 5–48. <https://doi.org/10.2151/jmsj.2015-001>
- Krzeminski, B., Bormann, N., Kelly, G., McNally, T., & Bauer, P. (2009). *Revision of the HIRS cloud detection at ECMWF (EUMETSAT/ECMWF fellowship Prog. Res. Rep. No. 19)*. ECMWF. Retrieved from <https://www.ecmwf.int/sites/default/files/elibrary/2009/10561-revision-hirs-cloud-detection-ecmwf.pdf>
- Liefhebber, F., Lammens, S., Brussee, P. W. G., Bos, A., John, V. O., Rührich, F., et al. (2020). Automatic quality control of the Meteosat First Generation measurements. *Atmospheric Measurement Techniques*, 13(3), 1167–1179. <https://doi.org/10.5194/amt-13-1167-2020>
- Lu, Q., & Bell, W. (2014). Characterizing Channel center frequencies in AMSU-A and MSU microwave sounding instruments. *Journal of Atmospheric and Oceanic Technology*, 31(8), 1713–1732. <https://doi.org/10.1175/JTECH-D-13-00136.1>
- Mahon, R., Greene, C., Cox, S.-A., Guido, Z., Gerlak, A. K., Petrie, J.-A., et al. (2019). Fit for purpose? Transforming national meteorological and hydrological services into national climate service centers. *Climate Services*, 13, 14–23. <https://doi.org/10.1016/j.cliser.2019.01.002>
- Masson-Delmotte, V., Zhai, P., Pirani, A., Connors, S. L., Péan, C., Berger, S., et al. (Eds.) (2021). *Climate change 2021: The physical science basis. Contribution of working Group I to the sixth assessment Report of the intergovernmental panel on climate change*. Cambridge University Press. <https://doi.org/10.1017/9781009157896>
- McCulloch, A. (2014). MRIR/Nimbus-3 level 1 meteorological radiation data V001 [Dataset]. NASA Goddard Earth Sciences Data and Information Services Center (GES DISC). <https://doi.org/10.5067/xtj53ak84qrl>
- Mears, C. A., & Wentz, F. J. (2017). A satellite-derived lower-tropospheric atmospheric temperature dataset using an optimized adjustment for diurnal effects. *Journal of Climate*, 30(19), 7695–7718. <https://doi.org/10.1175/JCLI-D-16-0768.1>
- Mitchell, T. M. (1997). *Machine learning*. McGraw-Hill.
- Munro, R., Lang, R., Klaes, D., Poli, G., Retscher, C., Lindstrot, R., et al. (2016). The GOME-2 instrument on the Metop series of satellites: Instrument design, calibration, and level 1 data processing—An overview. *Atmospheric Measurement Techniques*, 9(3), 1279–1301. <https://doi.org/10.5194/amt-9-1279-2016>
- National Research Council (U.S.) (Ed.). (2004). *Climate data records from environmental satellites*. National Academies Press.
- Nativi, S., Caron, J., Domenico, B., & Bigagli, L. (2008). Unidata's common data model mapping to the ISO 19123 data model. *Earth Science Informatics*, 1(2), 59–78. <https://doi.org/10.1007/s12145-008-0011-6>
- Newman, S., Carminati, F., Lawrence, H., Bormann, N., Salonen, K., & Bell, W. (2020). Assessment of new satellite missions within the Framework of numerical weather prediction. *Remote Sensing*, 12(10), 1580. <https://doi.org/10.3390/rs12101580>
- Njoku, E. (2003). Nimbus-7 SMMR pathfinder brightness temperatures, version 1 [Dataset]. NASA National Snow and Ice Data Center DAAC. <https://doi.org/10.5067/7Y1XWXT07HH8>
- Oertel, D., Spänkuch, D., Jahn, H., Becker-Ross, H., Stadthaus, W., Nopirakowski, J., et al. (1985). Infrared spectrometry of Venus from “Venera-15” and “Venera-16”. *Advances in Space Research*, 5(9), 25–36. [https://doi.org/10.1016/0273-1177\(85\)90267-4](https://doi.org/10.1016/0273-1177(85)90267-4)
- Pachot, C., Carnicero Domínguez, B., Sierk, B., Mariani, F., Riel, S., Oetjen, H., et al. (2021). Far infrared Fourier transform spectrometer breadboard activities for the FORUM mission, ESA's 9th Earth Explorer. In Z. Sodnik, B. Cugny, & N. Karafolas (Eds.), *International conference on space optics—ICSO 2020* (p. 75). SPIE. <https://doi.org/10.1117/12.2599355>
- Parker, H. R., Cornforth, R. J., Boyd, E., James, R., Otto, F. E. L., & Allen, M. R. (2015). Implications of event attribution for loss and damage policy. *Weather*, 70(9), 268–273. <https://doi.org/10.1002/wea.2542>
- Poli, P., Dee, D. P., Saunders, R., John, V. O., Rayner, P., Schulz, J., et al. (2017). Recent advances in satellite data rescue. *Bulletin of the American Meteorological Society*, 98(7), 1471–1484. <https://doi.org/10.1175/BAMS-D-15-00194.1>

- Poli, P., Hanschmann, T., Roebeling, R., Schulz, J., John, V., Théodore, B., et al. (2023). Brightness Temperature Spectra 400–1200 cm<sup>-1</sup> from satellite METEOR-29 instrument SI-1 in February 1979 along with radiative transfer simulations from 4 different reanalyses, clear scenes only over ocean [Dataset]. Zenodo. <https://doi.org/10.5281/zenodo.7912742>
- Poli, P., Hersbach, H., Dee, D. P., Berrisford, P., Simmons, A. J., Vitart, F., et al. (2016). ERA-20C: An atmospheric reanalysis of the twentieth century. *Journal of Climate*, 29(11), 4083–4097. <https://doi.org/10.1175/JCLI-D-15-0556.1>
- Privette, J. L., Wenying, S., Schulz, J., & Merchant, C. J. (2023). A definitions taxonomy for satellite climate data records and time series data sets (Vol. Poster session 1—other topics on climate variability and change (posters)). In *Presented at the American meteorological society—103rd AMS annual meeting, Denver, CO*. Retrieved from <https://ams.confex.com/ams/103ANNUAL/meetingapp.cgi/Program/1620>
- Quast, R., Giering, R., Govaerts, Y., Rüttrich, F., & Roebeling, R. (2019). Climate data records from Meteosat first generation Part II: Retrieval of the in-flight visible spectral response. *Remote Sensing*, 11(5), 480. <https://doi.org/10.3390/rs11050480>
- Rodgers, C. D. (1990). Characterization and error analysis of profiles retrieved from remote sounding measurements. *Journal of Geophysical Research*, 95(D5), 5587. <https://doi.org/10.1029/JD095iD05p05587>
- Rodgers, C. D., & Walshaw, C. D. (1963). Polynomial approximations to radiative functions. *Quarterly Journal of the Royal Meteorological Society*, 89(381), 422–423. <https://doi.org/10.1002/qj.49708938116>
- Ruti, P. M., Tarasova, O., Keller, J. H., Carmichael, G., Hov, Ø., Jones, S. C., et al. (2020). Advancing research for seamless Earth system prediction. *Bulletin of the American Meteorological Society*, 101(1), E23–E35. <https://doi.org/10.1175/BAMS-D-17-0302.1>
- Saunders, R., Hocking, J., Turner, E., Rayer, P., Rundle, D., Brunel, P., et al. (2018). An update on the RTTOV fast radiative transfer model (currently at version 12). *Geoscientific Model Development*, 11(7), 2717–2737. <https://doi.org/10.5194/gmd-11-2717-2018>
- Schipper, E. L. F. (2020). Maladaptation: When adaptation to climate change goes very wrong. *One Earth*, 3(4), 409–414. <https://doi.org/10.1016/j.oneear.2020.09.014>
- Schweiger, A. K., & Laliberté, E. (2022). Plant beta-diversity across biomes captured by imaging spectroscopy. *Nature Communications*, 13(1), 2767. <https://doi.org/10.1038/s41467-022-30369-6>
- Shahabadi, M. B., Aparicio, J. M., & Garand, L. (2018). Impact of slant-path radiative transfer in the simulation and assimilation of satellite radiances in environment Canada's weather forecast system. *Monthly Weather Review*, 146(12), 4357–4372. <https://doi.org/10.1175/MWR-D-18-0126.1>
- Stenchikov, G. L., Kirchner, I., Robock, A., Graf, H.-F., Antuña, J. C., Grainger, R. G., et al. (1998). Radiative forcing from the 1991 Mount Pinatubo volcanic eruption. *Journal of Geophysical Research*, 103(D12), 13837–13857. <https://doi.org/10.1029/98JD00693>
- Stephens, G. L. (1994). *Remote sensing of the lower atmosphere: An introduction*. Oxford University Press.
- Stöckli, R., Bojanowski, J. S., John, V. O., Duguay-Tetzlaff, A., Bourgeois, Q., Schulz, J., & Hollmann, R. (2019). Cloud detection with historical geostationary satellite sensors for climate applications. *Remote Sensing*, 11(9), 1052. <https://doi.org/10.3390/rs11091052>
- Swales, D. J., Pincus, R., & Bodas-Salcedo, A. (2018). The cloud feedback model intercomparison project observational simulator package: Version 2. *Geoscientific Model Development*, 11(1), 77–81. <https://doi.org/10.5194/gmd-11-77-2018>
- Théodore, B., Coppens, D., Doehler, W., Damiano, A., Oertel, D., Klaes, D., et al. (2015). A glimpse into the past: Rescuing hyperspectral SI-1 data from meteor-28 and 29. In *Presented at the EUMETSAT meteorological satellite conference*. EUMETSAT.
- Thorpe, A., & Rogers, D. (2018). The future of the global weather enterprise: Opportunities and risks. *Bulletin of the American Meteorological Society*, 99(10), 2003–2008. <https://doi.org/10.1175/BAMS-D-17-0194.1>
- Watkin, S. C. (2003). The application of AVHRR data for the detection of volcanic ash in a Volcanic Ash Advisory Centre: Application of AVHRR data in volcanic ash detection. *Meteorological Applications*, 10(4), 301–311. <https://doi.org/10.1017/S1350482703001063>
- WCC-3. (2009a). Conference declaration. Retrieved from [https://gfcs.wmo.int/sites/default/files/WCC3\\_declaration\\_en.pdf](https://gfcs.wmo.int/sites/default/files/WCC3_declaration_en.pdf)
- WCC-3. (2009b). Conference statement. Retrieved from [https://gfcs.wmo.int/sites/default/files/WCC-3\\_Statement\\_07-09-09mods.pdf](https://gfcs.wmo.int/sites/default/files/WCC-3_Statement_07-09-09mods.pdf)
- Wickham, H. (2011). The split-apply-combine strategy for data analysis. *Journal of Statistical Software*, 40(1), 1–29. <https://doi.org/10.18637/jss.v040.i01>
- World Meteorological Organization (WMO). (2018). *Step-by-step guidelines for establishing a national Framework for climate services*. WMO. Retrieved from [https://library.wmo.int/doc\\_num.php?explnum\\_id=4335](https://library.wmo.int/doc_num.php?explnum_id=4335)
- World Meteorological Organization (WMO), & European Commission. (2015). *Satellites for climate services: Case studies for establishing an architecture for climate monitoring from space*. WMO. Retrieved from [https://library.wmo.int/index.php?lvl=notice\\_display&id=18883](https://library.wmo.int/index.php?lvl=notice_display&id=18883)
- World Meteorological Organization (WMO), United Nations Educational Scientific and Cultural Organization (UNESCO), Intergovernmental Oceanographic Commission (IOC), United Nations Environment Programme (UNEP), & International Science Council (ISC). (2022). *The 2022 GCOS implementation plan*. WMO. Retrieved from [https://library.wmo.int/index.php?lvl=notice\\_display&id=22134](https://library.wmo.int/index.php?lvl=notice_display&id=22134)

## References From the Supporting Information

- Aires, F., Prigent, C., Bernardo, F., Jiménez, C., Saunders, R., & Brunel, P. (2011). A Tool to Estimate Land-Surface Emissivities at Microwave frequencies (TELSEM) for use in numerical weather prediction. *Quarterly Journal of the Royal Meteorological Society*, 137(656), 690–699. <https://doi.org/10.1002/qj.803>
- Borbas, E., & Feltz, M. (2019). *Updating the CAMEL surface emissivity atlas for RTTOV (report of visiting scientist mission No. NWP\_AS18\_01, NWPSAF-MO-VS-058, version 1.0)*. EUMETSAT NWP-SAF. Retrieved from [https://nwp-saf.eumetsat.int/publications/vs\\_reports/nwpsaf-mo-vs-058.pdf](https://nwp-saf.eumetsat.int/publications/vs_reports/nwpsaf-mo-vs-058.pdf)
- Kazumori, M., & English, S. J. (2015). Use of the ocean surface wind direction signal in microwave radiance assimilation. *Quarterly Journal of the Royal Meteorological Society*, 141(689), 1354–1375. <https://doi.org/10.1002/qj.2445>
- Saunders, R., Hocking, J., Rundle, D., Rayer, P., Havemann, S., Matricardi, M., et al. (2017). *RTTOV v12 science and validation report (Report of Visiting Scientist mission no. NWPSAF-MO-TV-41)*. EUMETSAT NWP-SAF. Retrieved from [https://www.nwpsaf.eu/site/download/documentation/rtm/docs\\_rttov12/rttov12\\_svr.pdf.78](https://www.nwpsaf.eu/site/download/documentation/rtm/docs_rttov12/rttov12_svr.pdf.78)
- Tans, P., & Keeling, R. (2021). Trends in atmospheric carbon dioxide [Dataset]. NOAA Global Monitoring Laboratory, Earth System Research Laboratories. Retrieved from <https://gml.noaa.gov/ccgg/trends/data.html>
- Vidot, J., Brunel, P., Dumont, M., Carmagnola, C., & Hocking, J. (2017). The VIS/NIR land and snow BRDF Atlas for RTTOV: Comparison between MODIS MCD43C1 C5 and C6. *Remote Sensing*, 10(2), 21. <https://doi.org/10.3390/rs10010021>